Scale Interactions Involved in the Initiation, Structure, and Evolution of the 15 December 1992 MCS Observed during TOGA COARE. Part I: Synoptic-Scale Processes

Alain Protat, Yvon Lemaître

Scale Interactions Involved in the Initiation, Structure, and Evolution of the 15 December 1992 MCS Observed during TOGA COARE. Part I: Synoptic-Scale Processes

A. PROTAT AND Y. LEMAÎTRE

Centre d'études des Environnements Terrestre et Planétaires, Velizy, France

(Manuscript received 20 January 2000, in final form 30 October 2000)

ABSTRACT

This paper, the first of a series, examines the synoptic-scale mechanisms involved in the initiation, structure, and evolution of a mesoscale convective system observed during TOGA COARE. This study relies upon the use of the Japanese *Geosynchronous Meteorological Satellite-4* imagery and ECMWF model outputs, from which diagnostic parameters are derived and interpreted. This mesoscale convective system consists initially of two groups of convective entities that progressively move toward each other and merge. It is shown that the synoptic-scale flow creates a favorable environment for the formation of this large convective system through the production of convective available potential energy (CAPE) by horizontal advection and the enhancement of low-level convergence in the region where the convective system formed. Moreover, the general evolution of the system is found to be governed by the synoptic-scale circulation and, more precisely, by the temporal evolution of CAPE and low-level convergence. The mechanisms leading to the initiation and general evolution of the system are examined. The easterly equatorial jet at 500 hPa triggered positive potential vorticity areas that propagated westward and generated an anticyclonic circulation. This anticyclonic circulation was enhanced during the development phase of the convective system through vortex stretching and tilting, which accelerated the low-level westerlies (corresponding to the southern branch of this circulation) and enhanced the low-level convergence associated with the studied convective system.

In a companion paper, the mesoscale and convective-scale processes involved in the internal organization of this mesoscale convective system are examined using the airborne Doppler radar dataset collected within the system from 1700 to 2100 UTC. The downscale interactions (i.e., from synoptic scale to mesoscale and convective scale) are scrutinized using both the synoptic-scale context described in this paper and the mesoscale and convective-scale characteristics derived from the airborne radar observations.

1. Introduction

Convection exhibits a broad spectrum of temporal and spatial scales. As a result, the interaction between the different scales of motion is one of the most crucial problems of meteorological concern, in both tropical and midlatitude regions. Numerous studies (e.g., Madden and Julian 1971, 1972, 1994; Nakazawa 1988; Young and Sikdar 1973; Liebmann and Hendon 1990; Sui and Lau 1992; Mapes and Houze 1993; Hendon and Salby 1994; Salby et al. 1994) done in the past on western Pacific convection focused on the coupling between the 30–60-day Madden–Julian oscillations (hereafter referred to as MJO), westerly wind bursts (as defined by Luther et al. 1983), and enhanced convection, revealing the complexity of the convection-organized synoptic-scale systems. These past studies evidenced that the largest component of such convection-organized large-scale systems was an eastward-propagating MJO. Another large-scale convective cloud feature over the equator, called the super cloud cluster (SCC), was found to be associated with eastward-propagating atmospheric waves. These super cloud clusters exhibit an internal cloud substructure (as noted by several authors, e.g., Nakazawa 1988; Chen and Houze 1997), characterized by westward-moving cloud clusters. Furthermore, these studies permitted identification of a modulation of convective activity by 3–5 days' period easterly waves, which have been categorized in various types (tropical depression–type disturbances, Rossby–gravity wave–type disturbances, inertio–gravity waves, etc.) by several authors (e.g., Takayabu and Nitta 1993; Liebmann and Hendon 1990).

The evidence of cloud systems in large-scale atmospheric disturbances indicates the existence of mechanisms of coupling between deep convection and atmospheric waves. Numerous theoretical and numerical works investigated the processes responsible for such coupling (i.e., Charney and Eliassen 1964; Hayashi 1970). In these works, it is assumed that organized con-

Corresponding author address: Dr. Alain Protat, CETP–UVSQ, 10–12 Avenue de l'Europe, 78140 Vélizy, France.
E-mail: protat@cetp.ipsl.fr

vective motions and associated heating force the atmospheric disturbances through diabatic heating, and that the resulting atmospheric disturbances subsequently provide synoptic-scale conditions favorable for the development of convective motions. However the lack of suitable observational datasets (lack of sufficient surface and upper air data) did not allow such mechanisms to be scrutinized.

In this context, the Tropical Ocean Global Atmosphere Coupled Ocean–Atmosphere Response Experiment (TOGA COARE) was conducted in the western equatorial Pacific Ocean (Webster and Lukas 1992). Since clouds are a key link in the interaction of ocean and atmosphere, one of the major objectives of COARE was to document the behavior of clouds at different time and space scales, including the understanding of cloud organization; the estimate of apparent sources of heat, moisture and momentum; and understanding of cloud effects on the ocean through surface fluxes and precipitation. International efforts focused during the Intensive Observing Period (IOP) of COARE (from Nov 1992 through Feb 1993) on the description and understanding of the atmospheric processes that organize convection in this warm pool region, and the multiple-scale interactions that extend the atmospheric influence of the western warm pool systems to other regions and vice versa.

Among the numerous results obtained using the COARE dataset, let us recall briefly those devoted to scale interactions between convection and large-scale flow. Deep convection in the western Pacific warm pool appears to be organized the same way as in other parts of the Tropics, occurring in cloud clusters that are often observed to group together (Nakazawa 1995; Mapes and Houze 1993). This reflects in particular the most prominent large-scale circulation structure associated with the tropical intraseasonal oscillation or the MJO, whose convective activity is strongly connected with a quasi-2-day wave (Takayabu et al. 1996). As noted by several authors, the eastward-propagating SCCs observed during the COARE IOP had an internal structure (e.g., Chen and Houze 1997), consisting of generally westward moving cloud clusters embedded in these 2-day disturbances. However, some of these cloud clusters were stationary, and some propagated eastward (Chen et al. 1996). These eastward-propagating active convective episodes were followed by suppressed high-cloudiness episodes associated with anomalous low-level easterlies [the potential causes for these convective inhibition periods were studied extensively by Numaguti et al. (1995), Johnson et al. (1996), and Mapes and Zuidema (1996)]. The convective activity was found to be enhanced 1–3 weeks prior to the three peak westerly wind bursts that occurred during COARE (Gutzler et al. 1994; McBride et al. 1995; Lin and Johnson 1996; Chen et al. 1996). These westerlies were lying between the double cyclonic gyres associated with Rossby wave–like disturbances (Chen et al. 1996). Diurnal heating of the atmosphere and ocean surfaces provides favored conditions in the afternoon for the formation of the cloud systems (Chen and Houze 1997). The deep convective variability is modulated by equatorial waves, as shown by the complex principal component analysis of Pires et al. (1997). Finally, statistical classification studies of convection evidenced four categories, linked to the mesoscale dimension and linear organization (Rickenbach and Rutledge 1998).

These TOGA COARE studies confirmed that large-scale atmospheric waves were strongly related to the convective activity. However, although this strong interaction between convection and large-scale flow is well established from the previous statistical studies, little is yet known regarding the respective role of each scale (from large scale to convective scale) and their interactions in the formation, general evolution, internal evolution, and propagative behavior of a Mesoscale Convective System (MCS). These crucial issues are the motivations of the present study. We attempt to examine this problem from a perspective differing from a statistical analysis of the whole TOGA COARE dataset, by selecting individual cloud clusters observed during COARE and by (i) accessing a complete description of the kinematic and dynamic fields at synoptic scale, mesoscale, and convective scale, within individual cloud clusters, (ii) examining for each scale of motion the kinematic and/or dynamic processes involved in the initiation, structure, evolution, and propagative behavior of these individual case studies, and (iii) studying the downscale interactions involved in the life cycle of these MCSs. This procedure is applied in this paper as well as Protat and Lemaitre (2001, hereafter Part II) to the 15 December 1992 cloud cluster, whose scientific interest will be discussed in the next sections. This work will then be followed by similar studies of other individual cases extracted from the TOGA COARE dataset [see preliminary results of Caillault et al. (1998) for the 12 December 1992 case study], characterized by spatial scales and propagative behaviors significantly different from the 15 December 1992 case.

The first part of this study (presented in this paper) describes the synoptic-scale atmospheric context of the 15 December 1992 cloud cluster. Then, Part II examines the mechanisms involved in the internal organization of this cloud cluster on the mesoscale and convective scale (using rawindsonde and airborne Doppler radar data), and examines their link with the synoptic-scale features in order to evaluate the downscale interaction processes involved in the 15 December system.

In section 2 of this paper, the quality of the ECMWF model outputs is evaluated for the 15 December 1992 day using the available radiosondes. Section 3 presents a brief overview of the larger-scale context in which the cloud cluster developed. The morphological evolution of the studied MCS is then examined in section 4 using the satellite imagery. In section 5, the synoptic-scale dynamic processes involved in the life cycle of this MCS are investigated. Finally, section 6 gives a summary, as well as concluding remarks.

2. Evaluation of the ECMWF model outputs

The European Centre for Medium-Range Weather Forecasts (ECMWF) analyses and Geosynchronous Meteorological Satellite (GMS) images are used in the present paper to describe the synoptic-scale context of the studied cloud cluster. The GMS brightness temperature data in the infrared channel are used to follow the evolution of the convective activity. These data are collected every hour, with a spatial resolution of approximately 11 km. The ECMWF analysis scheme is a four-dimensional data assimilation system in which multivariate observed data are combined with a first guess (a 6-h range forecast) using 3D optimal interpolation [see Nuret and Chong (1996) for further details]. Assimilated observations in the TOGA COARE area are wind, geopotential, pressure, and humidity measurements from 1) single-level land-based, ship-based, and drifting buoy data; 2) upper-air single-level data from indirect satellite estimation or aircraft; and 3) upper-air multilevel data from radiosonde soundings or wind soundings. At the time of TOGA COARE, information provided by polar-orbiting satellite was not used in the assimilation process.

The ECMWF model provides gridded fields (grid points every $1° \times 1°$) of the horizontal wind components, the vertical wind component expressed in pressure units, horizontal divergence, vertical component of vorticity (referred to as ''vertical vorticity'' in the following), relative humidity, and potential temperature. It is a 10-level analysis (1000, 850, 700, 500, 400, 300, 250, 200, 150 and 100 hPa, respectively) provided every 6 h. From the previous ''raw fields,'' other useful diagnostic quantities are computed and interpreted in this study, such as the equivalent potential temperature θ_e, the potential vorticity (denoted PV in the following), the convective available potential energy (CAPE), and the local temporal evolution (tendency term) of physical quantities, whose potential will be discussed hereafter. While interpreting those ECMWF fields, caution should be carefully exercised so that the gridpoint-scale local maxima and minima be not trusted as ''real'' structures. Indeed, those details are most likely model produced, rather than small-scale structures imposed by observations assimilated in the model. As a result, it must be clearly stated here that all we expect from the model in this study is a quite realistic description of the synoptic-scale dynamic characteristics of the atmosphere.

Nuret and Chong (1996) have performed a statistical quality control of the ECMWF outputs for the whole TOGA COARE IOP. The performances of this ECMWF model in midlatitude regions had already been evaluated, in particular by Hollingsworth (1994), who demonstrated the good accuracy of the retrieved fields, and pointed out some problems, such as biases on the relative humidity field, or difficulties to represent the wind field on the boundaries. In tropical regions, Nuret and Chong (1996) used the data collected during the TOGA COARE IOP in order to compare observations and analyses of the wind, temperature, and mixing ratio. These authors showed that (i) biases of about 1 m s^{-1} occurred for the horizontal wind, with a maximum of 1.5 m s^{-1} within the strong upper-level easterly jet, (ii) the analysis was too moist in the lower troposphere, and too dry in midtroposphere, with a maximum bias of 0.5 g kg^{-1} at 500 hPa for the mixing ratio (corresponding to a 10% underestimation of relative humidity), (iii) biases on temperature are less than 0.5°C, and (iv) the standard deviation of the difference between model outputs and observations computed for the whole TOGA COARE IOP was quite large (e.g., 3–4 m s^{-1} for the horizontal wind).

This large standard deviation clearly shows that the quality of the outputs strongly depends on the day of analysis within the IOP. Therefore, an evaluation of the 15 December 1992 ECMWF outputs is carried out in what follows using the few radiosoundings available in the domain of interest. This comparison between model outputs and the six radiosoundings available for this day in the COARE domain is displayed in Figs. 1a–c for the horizontal wind, potential temperature, and equivalent potential temperature, respectively. This comparison includes the mean difference between observations and model data (solid line in Fig. 1) and the standard deviation of this difference (error bars in Fig. 1). It must be noted that known biases in the sounding measurements were not subtracted. These biases are therefore included in the calculated differences.

The vertical profiles of horizontal wind and potential temperature exhibit mean differences of less than 1 m s^{-1} and 1°C, respectively, which correspond to the averaged biases found in Nuret and Chong (1996). The standard deviation is of about 2 m s^{-1} for the horizontal wind difference and about 1.5 K for the potential temperature. The larger mean difference observed below 700 hPa on the θ_e vertical profile (Fig. 1c) is due to both the errors on the ECMWF analysis of relative humidity and the biases on the Vaisala sounding measurements of relative humidity in the low levels (recently detected by Zipser and Johnson 1998). It must be noted however that the present error analysis is particularly demanding for the model, since a comparison is done between the model at one grid point and the sounding data at the same location (much within the grid resolution of the model).

3. Large-scale context of the 15 December 1992 cloud cluster

The 15 December 1992 cloud cluster developed when westerly winds began to appear in the lowest tropospheric layers in association with the second major westerly wind burst episode of COARE [see Gutzler et al.

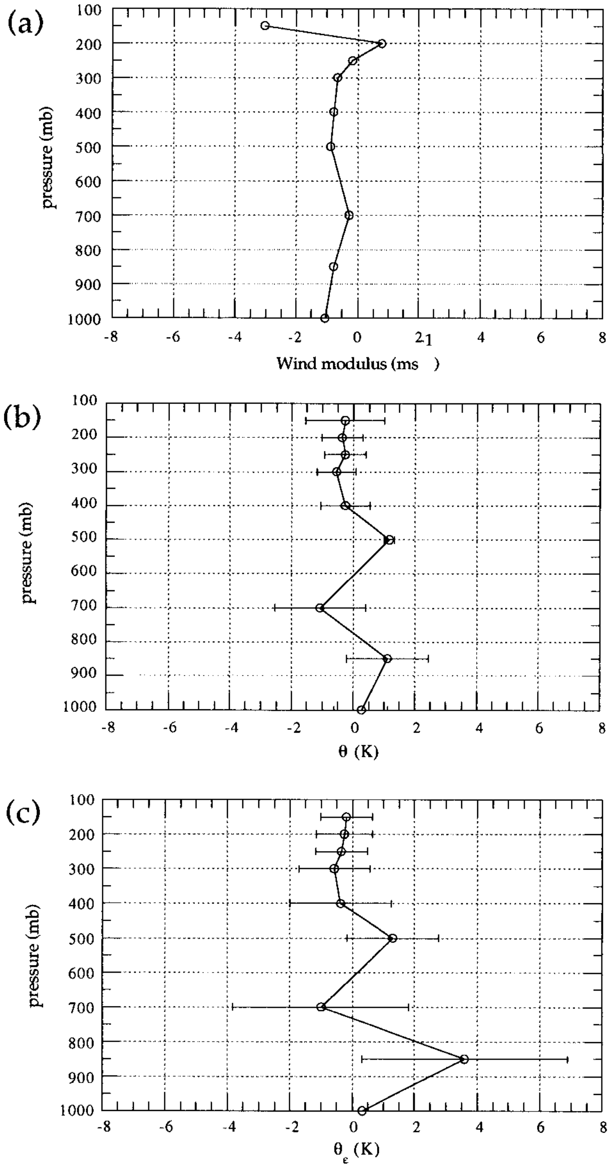

FIG. 1. Vertical profile of the ECMWF–radiosoundings difference fields of (a) horizontal wind, (b) potential temperature, and (c) equivalent potential temperature. Horizontal bars represent standard deviation of this difference for every height.

(1994), McBride et al. (1995), Lin and Johnson (1996), and Chen et al. (1996) for more details about the large-scale flow during TOGA COARE]. More precisely, this cloud cluster appeared 2 weeks prior to the peak westerly winds (1 Jan 1993). This is consistent with the findings of Lin and Johnson (1996), who document a maximum occurence of deep convection 1–3 weeks prior to the westerly wind burst maxima of the COARE IOP.

Figures 2a and 2b show the ECMWF analysis of horizontal wind at 0600 UTC (all times are UTC in the following), for the 250- and 850-hPa levels, respectively. The 250-hPa analysis (Fig. 2a) is mainly characterized by two anticyclonic gyres, denoted A_1 and A_2 in Fig. 2a, and two troughs located, respectively, around 178°E in the Northern Hemisphere and around 160°E in the Southern Hemisphere. In the low levels (Fig. 2b), the northeasterly trade winds have been accelerated in the Northern Hemisphere by a depression (D in Fig. 2b) observed a few days previously (Bonnissent et al. 1993). In the Southern Hemisphere, a southeasterly flow regime dominates. This southeasterly flow has been reinforced by the presence of Tropical Cyclone Joni, denoted J in Fig. 2b (see McBride et al. 1995) and located near (25°S, 178°E). As this southeasterly flow approached the TOGA COARE Intensive Flux Array (IFA), its direction changed to southwesterly. A synoptic-scale equatorial convergence was initiated west of 160°E between this southwesterly flow and the trade winds in the Northern Hemisphere.

These circulations at 850 and 250 hPa may be compared to the 11-yr composite analysis of the MJO performed by Hendon and Salby (1994) (analyses at 850 and 200 hPa, see their Fig. 5) in order to examine the possible presence of an active phase of MJO at that time. Their 200-hPa analysis is characterized by two anticyclonic circulations separated by a well-defined easterly signature, while westerly winds are found in the low levels (their Fig. 5). These results are fairly comparable to the synoptic-scale circulations of Fig. 2, despite the fact that Figs. 2a and 2b are a 6-h analysis of a total field, while the fields shown in Hendon and Salby (1994) are deviations from a basic state of the troposphere on an 11-yr average. Hence, according to the findings of Hendon and Salby (1994), the A_1 and A_2 vortices of Fig. 2a may be interpreted as the dynamic response of the atmosphere (under the form of Rossby waves) to an earlier convective activity that developed near the equator, weakened, and moved southward. These results are confirmed by the presence of convection near the equator on 9 December (as discussed in Chen et al. 1996), which collapsed prior to 15 December. It must be noted as well that this presence of Rossby waves, deduced from this simple comparison, is in good agreement with the results of Pires et al. (1997), who detected equatorially trapped Rossby waves at the same time using a complex principal component analysis.

4. Morphology and evolution of the 15 December cloud cover

The multiscale variability of deep convection in relation to large-scale circulation during the COARE IOP is documented by Chen et al. (1996), who analyze the satellite-observed data in terms of both the continuous mean cloudiness and discrete ‘‘cloud cluster’’ points of view. According to this study, the 15 December cloud cluster appears as one of the most active convection in COARE, characterized by one of the largest spatial scale [class 4 system according to the 208-K infrared temperature threshold discussed in Mapes and Houze

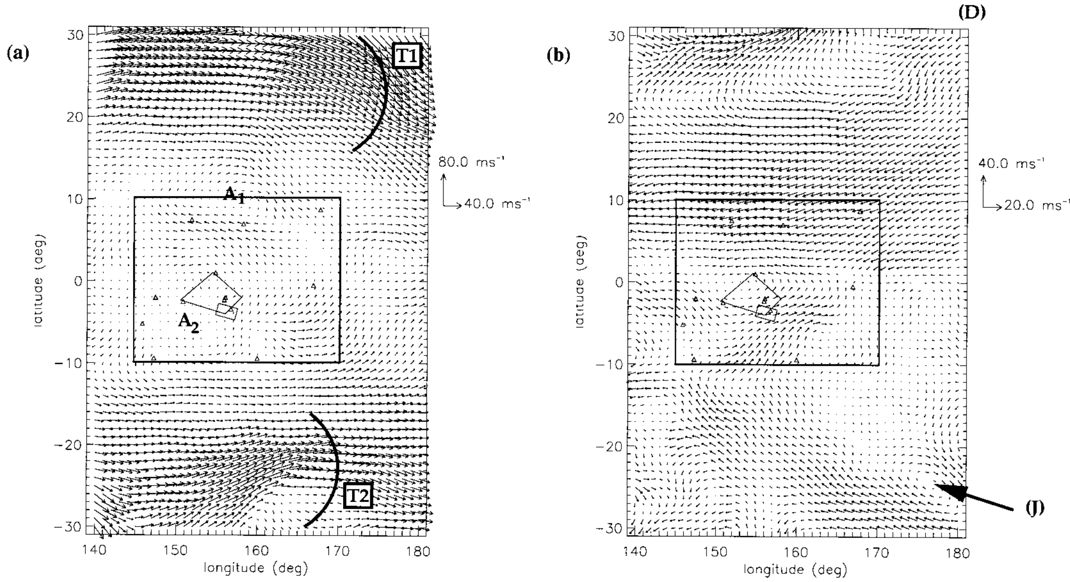

FIG. 2. The 15 Dec 1992 ECMWF analysis of the horizontal wind at 0600 UTC and at (a) 250 and (b) 850 hPa. The locations of two anticyclonic vortices, A_1 and A_2, and two troughs, T_1 and T_2, are indicated in (a). The locations of a pressure low observed 2 days earlier (D), and of Tropical Cyclone Joni (J), are indicated in (b). The triangles represent the radiosoundings available from 0000 to 2400 UTC on 15 Dec 1992. The trapeziod shows the IFA, and the rectangle on its southeastern border corresponds to the area covered by the airborne Doppler radars involved in TOGA COARE. The larger rectangle represents the large-scale area chosen for the following further interpretation.

(1993)]. Contrary to the common westward-propagating clusters, it is found that this cloud cluster remains zonally stationary (Chen et al. 1996).

In this section, we examine a sequence of satellite images in order to describe the life cycle of this particularly interesting cloud cluster and associated individual convective entities. Figure 3 shows the brightness temperature fields in the infrared channel of the *GMS-4* satellite for 15 December 1992 at 0631, 0931, 1131, 1331, 1623, 1800, 2031, and 2331 UTC. The 208-K threshold for infrared brightness temperatures represents a close approximation to the boundary of the precipitating core of tropical convective systems (e. g., Chen et al. 1996). However, it must be noted that light gray shadings characteristic of infrared brightness temperatures less than about 250 K should be interpreted as possible deep convection as well (Chen et al. 1996).

At 0631 (Fig. 3a), the convective activity is mostly concentrated along a northwest–southeast axis in the Southern Hemisphere. Inspection of the monthly averaged cloudiness during COARE, studied by Bonnissent et al. (1993), Gutzler et al. (1994), Lin and Johnson (1996), and Chen et al. (1996), showed that the month of December was characterized by a large single cloud band south of the equator (whose location is the same as that of the convective activity discussed just above), associated with the South Pacific convergence zone (SPCZ), while convection was suppressed within the inter tropical convergence zone at that time. The location of this South Pacific convergence zone in December, deduced from the studies mentioned previously, is drawn in Fig. 3.

The most intense convective system along this South Pacific Convergence zone is located around (8°S, 158°E). Other less developed convective entities are also seen in the domain, located roughly along the equator. These latter entities progressively intensify and organize themselves from 0631 to 0931 along a well-defined convergence line roughly oriented along a W–E axis (dashed line denoted as ECZ, for equatorial convergence zone, in Figs. 3a–c). Convective entities, roughly oriented along a southwest–northeast axis denoted L1 in the following (see Fig. 3b), are triggered on the south-southeastern border of a convective system located in the northern part of the IFA, inducing an apparent southeastward propagation of this system. Meanwhile, the convective system located around (8°S, 158°E) experiences an apparent northwestward propagation from 0631 to 1131 (Figs. 3a–c). This apparent propagation arises from the triggering of new convective cells on its north-northwestern border that progressively get roughly organized along a southwest–northeast axis. Also noteworthy is the existence of a cloud cluster east of the IFA around (2°S, 161°E). From 1131 UTC (Fig. 3c) to 1331 UTC (Fig. 3d), the convective entities triggered north-northwest of the convective system around (8°S, 158°E) and the cloud cluster located east of the IFA gets progressively aligned along a second southwest–northeast axis denoted L2 in the following. The propagations of the previous convective entities (roughly aligned

(a)

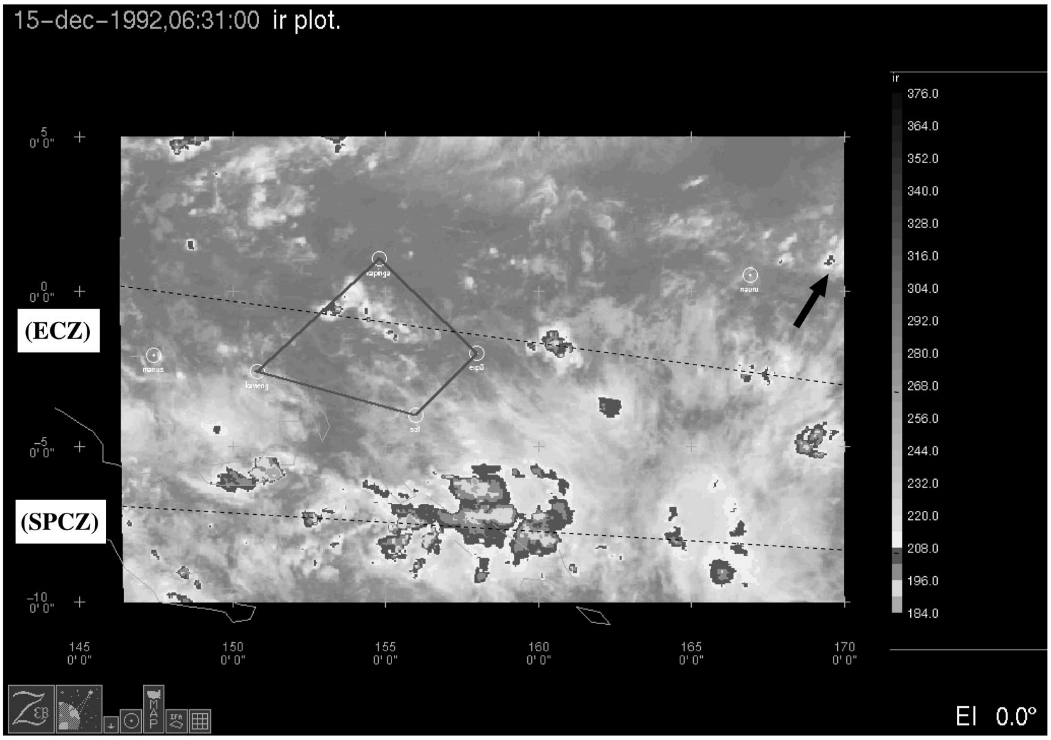

(b)

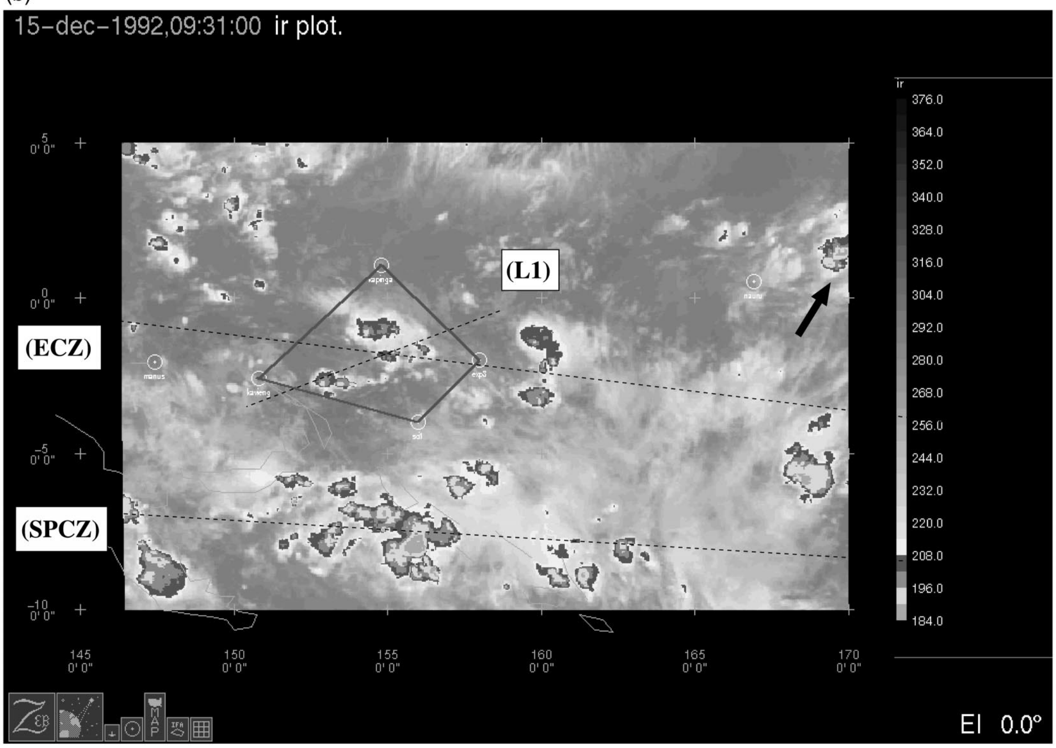

FIG. 3. Brightness temperature fields in the infrared channel of the *GMS-4* satellite at (a) 0631, (b) 0931, (c) 1131, (d) 1331, (e) 1623, (f) 1800, (g) 2031, and (h) 2331 (all times are UTC). Also indicated are two axes (L1) and (L2) along which convective entities are roughly oriented, two large-scale convergence lines (ECZ) and (SPCZ) in dashed lines (defined in the text), and the location of the MCS studied along this work (S) [(e) and (f)]. The arrow in (a)–(h) indicates the location of a squall line moving southwestward within the domain. The rectangle displayed in Fig. 3c corresponds to the area A defined in the text.

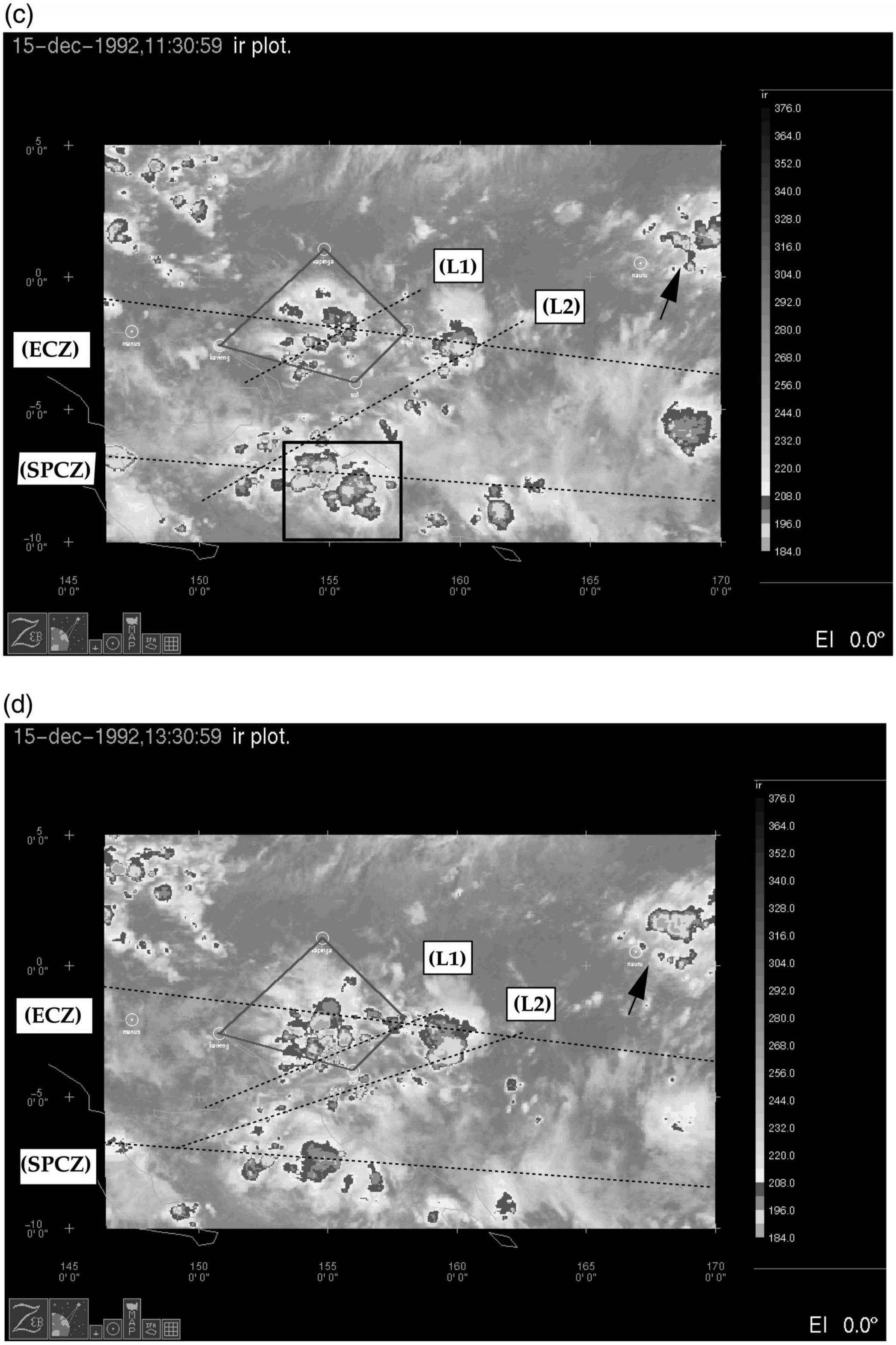

Fig. 3. (*Continued*)

(e)

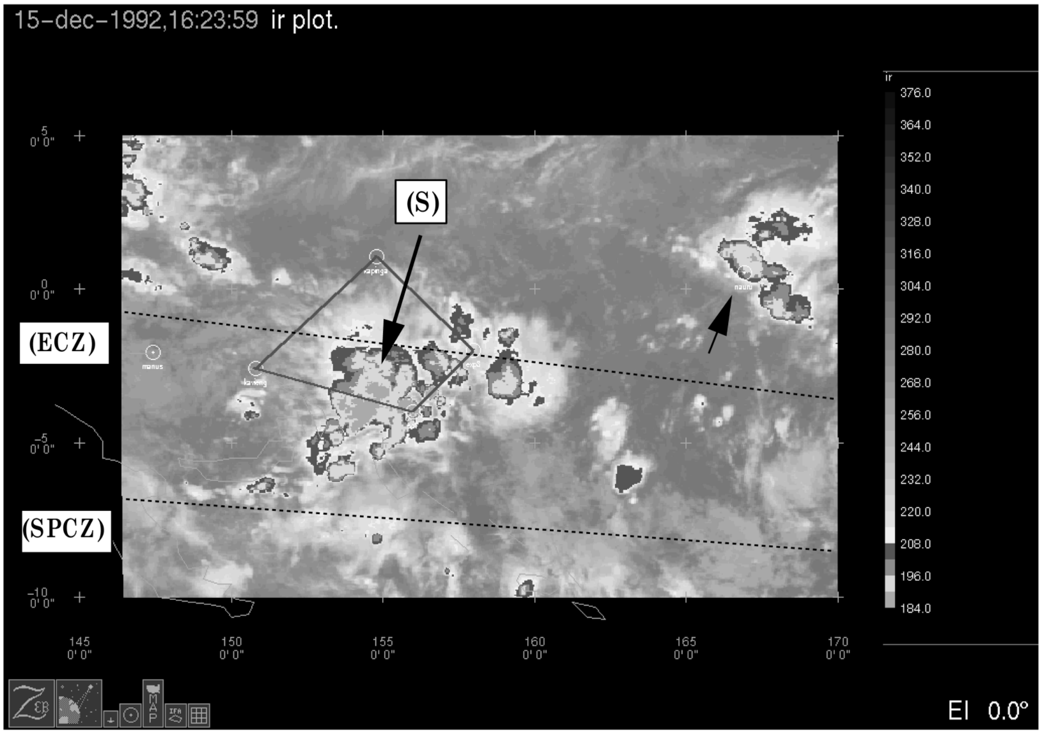

(f)

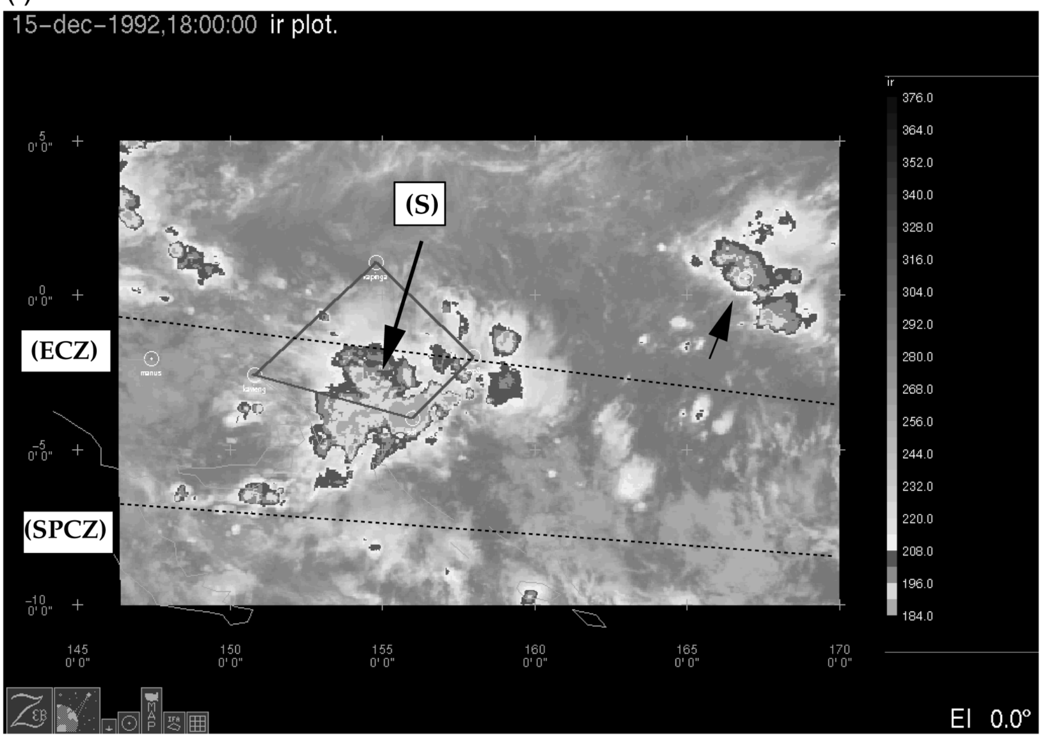

FIG. 3. (*Continued*)

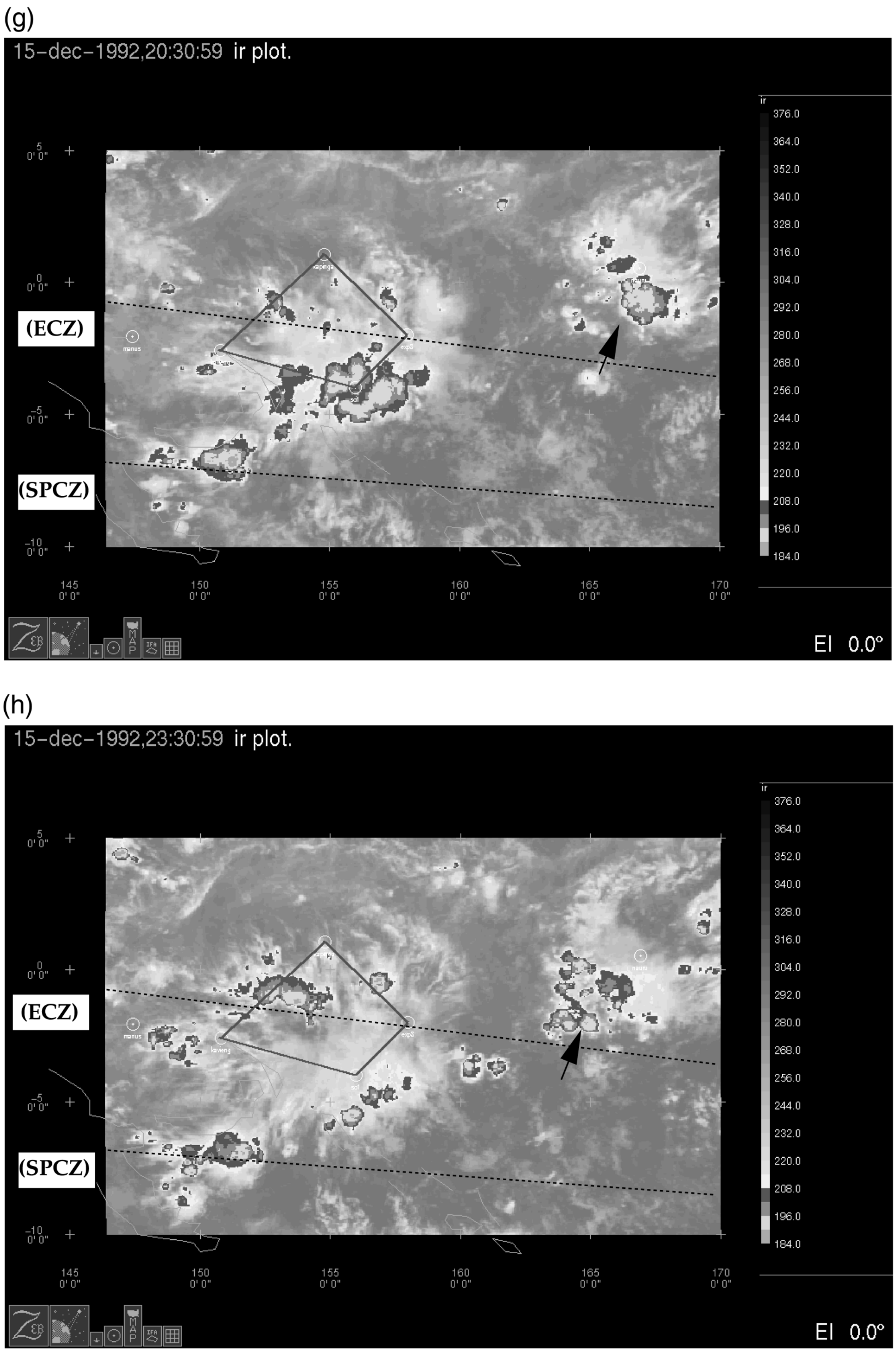

FIG. 3. (*Continued*)

along L1 and L2, respectively) lead to a progressive merging of these entities from 1331 (Fig. 3d) to 1631 (Fig. 3e). As these entities merge, convection is significantly enhanced in this area, as shown by the increasing size of the area where brightness temperatures are less than 208 K at 1131 (Fig. 3c). The MCS resulting from this merging (denoted S in the following; see Figs. 3e and 3f) reaches its mature stage around 1800 (Fig. 3f), which corresponds to the time at which two National Oceanic and Atmospheric Administration P3 aircraft carrying the Doppler radars [see Jorgensen et al. (1983) and Hildebrand and Mueller (1985) for further details about the airborne Doppler radars] started sampling the cloud cluster.

System S at 1800 consists of strong convective entities growing on its southeastern part, and a larger precipitating area on its northwestern part. Further details about the internal structure of S cannot be inferred from these GMS images. The reflectivity measurements of the Doppler radars will be used to describe the detailed morphological structure of S on the mesoscale and convective scale. These reflectivity fields indicate that S consists actually of two distinct convective systems, which are morphologically different. This will be investigated in more detail in Part II. From 1800 to 2031 (Figs. 3f and 3g), S is progressively dissipating. As a result, two convective systems are triggered northwest and southeast of S, respectively. At 2331 (Fig. 3h), S is almost completely dissipated. Two new groups of convective entities then form, oriented along a southwest–northeast axis, in the Southern Hemisphere and near the equator.

5. Synoptic-scale processes involved in the life cycle of the cloud cluster

In this section, we examine the dynamic and thermodynamic mechanisms involved in the initiation, evolution, and decay of the convective system denoted S in the previous section. For this purpose, the ECMWF analyses at 0600, 1200, 1800, and 2400 UTC are simultaneously interpreted.

a. *Identification of regions favorable at the synoptic scale for the development of convection*

The development of convective storms depends on the presence of environmental conditions favorable for the occurrence of deep convection. A tropical disturbance will develop in regions where the atmosphere is conditionally unstable. This tropospheric state can result from either a warming and/or moistening of the boundary layer (through advection or surface fluxes) or drying and cooling at midlevels. This leads to regions characterized by strong conditional convective instability. This convective instability will be released if a triggering mechanism acts to uplift the warm and moist air parcels up to their level of free convection (hereafter referred to as LFC). This triggering mechanism can be a synoptic-scale low-level convergence and/or a smaller-scale forcing, such as an interaction with a cold outflow generated by a preexisting convective system. The developing disturbance acts then as a thermodynamic stabilizer of the troposphere, releasing convective instability through replacement of boundary layer high-θ_e air with midtropospheric low-θ_e air and transport of the low-level available energy toward the upper troposphere (the so-called overturning process, that will be identified as such in the following discussions).

Several indices were developed to measure the susceptibility of a given temperature and moisture profile to the occurrence of deep convection. Among them, a particularly useful quantity is the CAPE, which corresponds to the maximum possible kinetic energy that a conditionally convectively unstable parcel uplifted to its LFC can acquire during its ascent between this LFC and the parcel equilibrium level. In the following, we will therefore analyze the ECMWF synoptic-scale CAPE and divergence fields. These fields are given in Figs. 4 and 5, respectively, in the same domain as the GMS images of Fig. 3, at 850 hPa and at 0600, 1200, 1800 and 2400 UTC. The CAPE fields (Fig. 4) exhibit positive values from 1200 to 1800 UTC in the area where S reaches its mature stage at 1800, that is, at the location of the mesoscale domain sampled by the airborne Doppler radars (see rectangle on the southeastern corner of the IFA in Fig. 4). It must be noted that the extremely large values found in the southwestern corner of the panels of Fig. 4 should obviously not be trusted (they appear on the low-level relative humidity field as well, with values exceeding 100%). As these large CAPE values are located over the southeastern part of Papua New Guinea, it is believed that they are due to an inadequate parameterization in the model over land. It should also be noted that the general overestimation of the CAPE is probably related to our use of only 10 levels of analysis and of a single horizontal plane (the 1000-hPa level, instead of the lowest 50 mb as is classically done) to compute CAPE.

Generally, the CAPE and brightness temperature fields of Figs. 3a,c,f,h do not exhibit the same spatial distribution. This is not surprising since a triggering mechanism (such as synoptic-scale low-level convergence) is required to uplift the parcels up to their LFC, as discussed previously. In addition, the computation of CAPE starting from the 850-hPa level shows nil or slightly negative values throughout the domain (not shown). This result indicates that the air parcels participating in convection are mainly located in the lowest levels. Hence, the potential occurrence of deep convection in areas characterized by both CAPE and low-level convergence is examined in the following.

The divergence field (Fig. 5) shows the existence of a convergence zone oriented along a southwest–northeast axis, in the region where the convective entities are roughly aligned along L2 at 1200 (Fig. 5b) and the

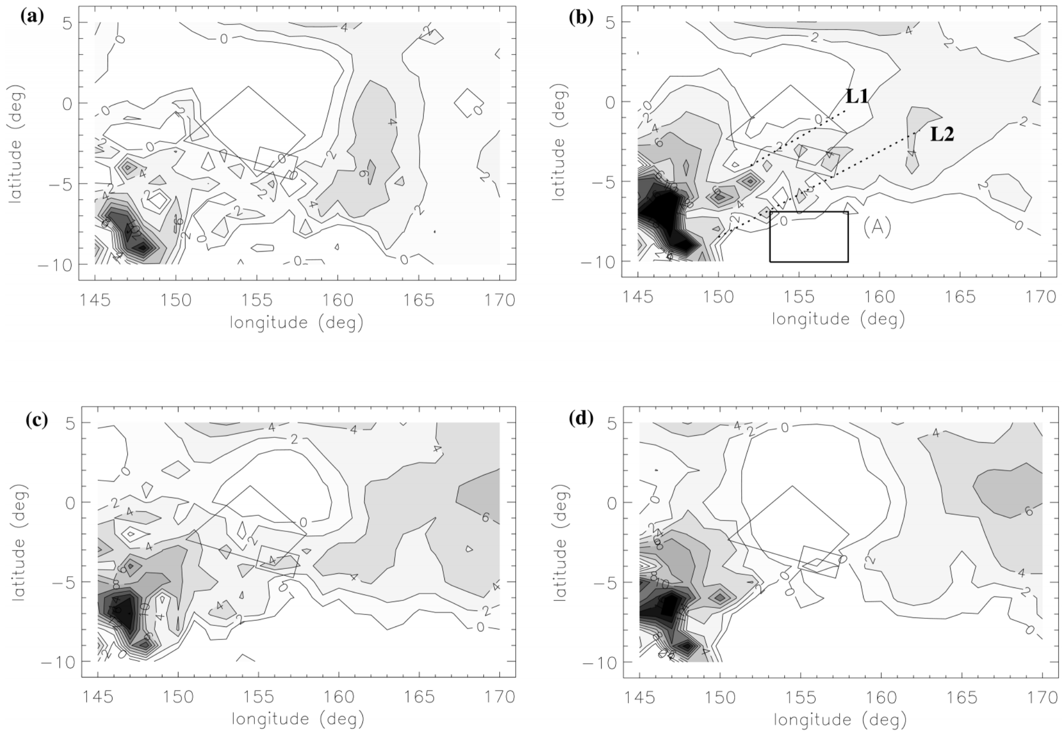

FIG. 4. The 15 Dec 1992 ECMWF analysis of the CAPE field (expressed in 10^3 J kg^{-1}) at (a) 0600, (b) 1200, (c) 1800, and (d) 2400 presented in the same domain as in Fig. 3. The large rectangle in (b) is the area A discussed in the text. The trapeziod is the IFA, and the small rectangle on its southeastern border corresponds to the area covered by the airborne radars involved in TOGA COARE. Also shown are the two axes, (L1) and (L2), of Fig. 3.

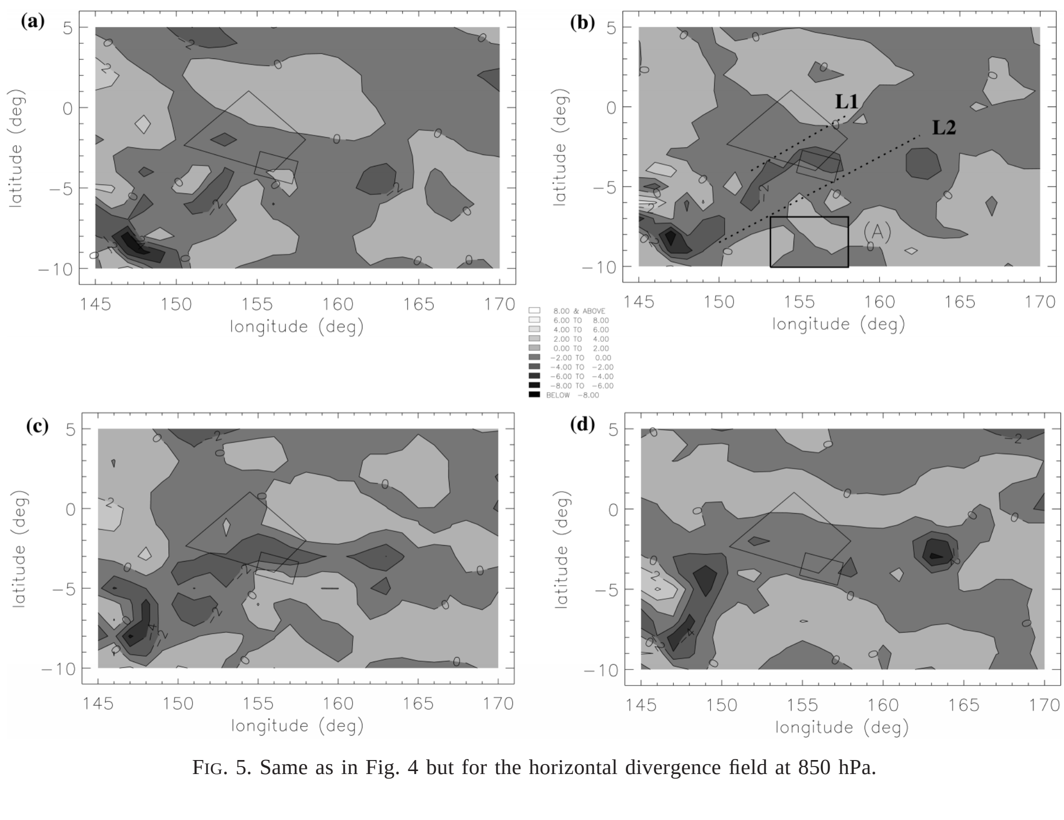

FIG. 5. Same as in Fig. 4 but for the horizontal divergence field at 850 hPa.

system S at 1800 develops. The magnitude of this convergence zone, which increases from 0600 to 1800 and decreases from 1800 to 2400, appears to be connected to the evolution of S observed on the satellite imagery. This convergence zone is characterized by positive CAPE (Fig. 4), whose magnitude increases from 0600 to 1800. At 2400, no more CAPE is observed in this area. This suggests that the overturning process (replacement of boundary layer air with midtropospheric air, as discussed in section 2) is achieved at that time, since all the warm, moist air in the low levels was transported to the upper troposphere between 1800 and 2400. This overturning leads to the decay of the system.

The superposition of positive CAPE and strong low-level convergence leads to a region particularly favorable for the development of convection, which is actually the region where S did form. This important result implies that the synoptic-scale dynamic features provided the initial conditions required for the development of S. In addition, the evolution of the CAPE and divergence fields in time are clearly in connection with the evolution of the convective activity within S observed in the satellite images of Fig. 3. This shows that the evolution of the synoptic-scale dynamic characteristics drives the general evolution of S as well.

In view of the previous results, further investigation of the synoptic-scale dynamic mechanisms responsible for the observed life cycle of S is carried out in what follows, but an interesting point could first be made about the combined use of the divergence, CAPE, and GMS fields. Indeed, while the convective activity is clearly related spatially to the areas where *both* CAPE and low-level convergence are present (cf. Figs. 3a,c,f,h with Figs. 4 and 5), convection is sometimes observed in regions of nil or slightly negative CAPE. As an example, the region A of Figs. 3c, 4b, and 5b is characterized by a well-developed convective system in a region of nil or slightly negative CAPE, except on its north-northwestern border where new convective cells are generated from 0631 to 1131 (Figs. 3a–c, and discussion of section 4). This may be hypothetically explained by the fact that this convective system already stabilized the troposphere through overturning at this time. According to this hypothesis, this system should enter its dissipating stage, which is indeed observed in Figs. 3d–f. This example illustrates the limitations of the combined examination of the divergence, CAPE, and GMS fields, since it cannot be inferred at a given time step whether the observed cloud clusters will be developing or dissipating. The temporal evolution of CAPE would in this respect be useful additional information to estimate at a given time step if the synoptic-scale circulation will subsequently promote or inhibit the convective activity, and by which process(es). For this purpose, we propose and apply in the following section a procedure to estimate qualitatively this CAPE tendency from the model fields at a given time step.

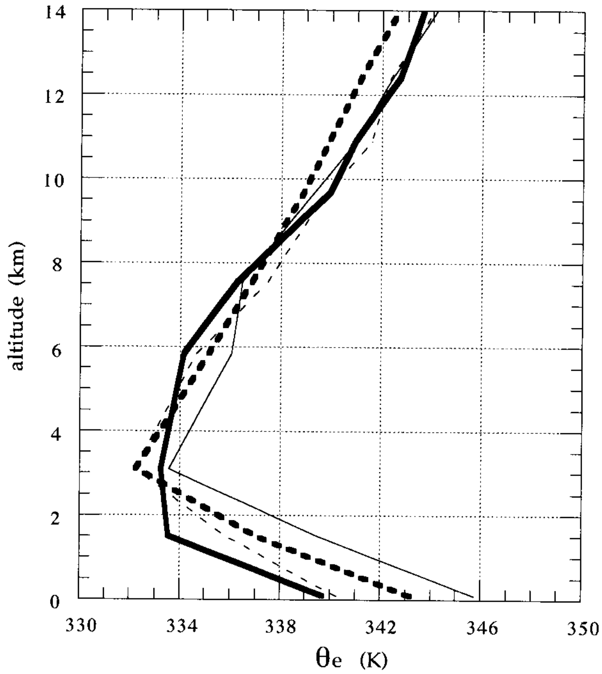

FIG. 6. Vertical profiles of equivalent potential temperature taken at (3°S, 155°E) and at 0600 (bold solid line), 1200 (thin solid line), 1800 (bold dashed line), and 2400 (thin dashed line).

b. Relationship between CAPE production and temporal evolution of S

Figure 6 shows the model-derived vertical profile of θ_e at the location where S formed (3°S, 155°E) and at the four times of ECMWF analysis. A negative vertical gradient of θ_e is found in the 1000–700 hPa layer at all times, whose slope is characterized by a significant temporal variability. In contrast, the vertical gradient of θ_e is positive above the 700-hPa level and almost constant in time. The negative θ_e gradient in the 1000–700-hPa layer significantly increases from 0600 to 1200 (from -5 to -9.5 K), constant from 1200 to 1800, and decreases from 1800 to 2400 (from -9.5 to -6 K). In contrast, the vertical gradients of moisture (not shown) in the 1000–700-hPa layer remain roughly the same from 0600 to 2400. Therefore, the evolution of CAPE seen in Fig. 4 is mostly due to the change in slope of the negative θ_e vertical gradient within the 1000–700-hPa vertical slab in the region where S develops. This can be explained theoretically as follows. On a θ_e vertical profile, a parcel is displaced along the iso-θ_e lines. CAPE is proportional to the surface bounded by the virtual potential temperature profiles θ_v representative of the environment and of the parcel, respectively. An increase of θ_e at ground level (due to an increase of temperature or moisture) would lead to an increase of the virtual potential temperature of the parcel, and therefore to an increase of this surface corresponding to CAPE. In the same way, a diminution of θ_e at 700 hPa (due to a corresponding diminution of temperature or

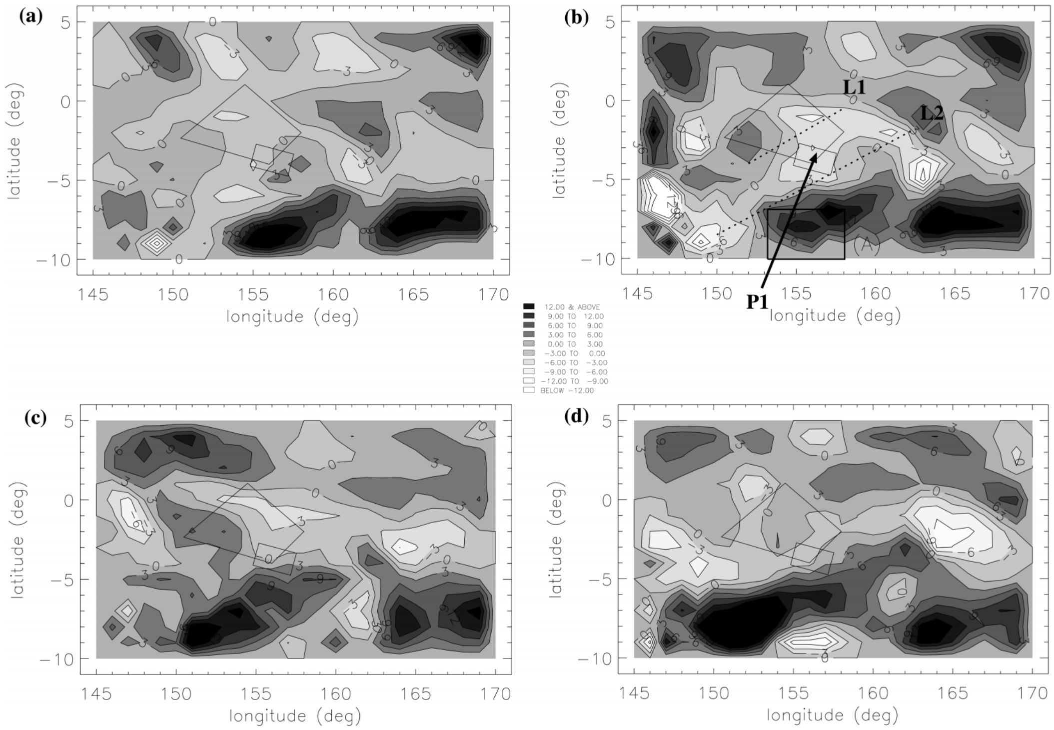

FIG. 7. Same as in Fig. 4 but for the CAPE tendency fields (using the vertical levels from 1000 to 700 hPa) at (a) 0600, (b) 1200, (c) 1800, and (d) 2400 presented in the same domain as in Fig. 3. Negative (positive) values indicate that CAPE is produced (diminishing). The location of the CAPE production area (P1) associated with (S) is also given.

moisture) would lead to a decrease of the virtual potential temperature of the environment and, hence, to an increase of CAPE. Therefore, the rate of change of this vertical θ_e gradient within the 1000–700-hPa vertical slab may be used *in our case* as a qualitative indicator of production or diminution of CAPE in time within the considered domain. However, it must be noted that this quantity does not correspond to the exact CAPE production, and should be considered as a qualitative estimate. By using this approach, the synoptic-scale thermodynamic processes contributing to the CAPE tendency can be estimated (and their relative importance assessed), as shown in the appendix. These processes are (i) advective terms related to the displacement of energy in a given direction, and (ii) differentially advective terms, which express the generation of CAPE through differential displacement with altitude of thermodynamically different air masses, leading to a vertical superposition of air masses favorable for the development of convection [see (A3) and further details of calculations in appendix]. It must be noted that this calculation of CAPE production by the synoptic-scale circulation does not include the possible contribution of surface energy fluxes that would arise from temperature or moisture contrasts in the synoptic-scale circulation at low levels. The surface latent and sensible heat fluxes have been estimated by Lin and Johnson (1996) for the December–January westerly wind burst episode. For 15 December 1992, values of about 50 and 10 W m^{-2} were obtained, respectively (see Fig. 16 of Lin and Johnson 1996). It may be shown that the corresponding production of CAPE is of about 1×10^{-8} K m^{-1} s^{-1}, which is three times less than the smallest structures interpreted hereafter. Therefore, this neglected contribution of the surface fluxes does not seem to play a significant role in the CAPE production.

These fields of ''CAPE production'' are given in Fig. 7 at 0600, 1200, 1800, and 2400 UTC. Let us recall that, as discussed in section 2, the gridpoint-scale local maxima and minima (see in particular the southwestern corner of Fig. 7) may not be realistic, since these features are most likely model products, rather than small-scale structures imposed by observations assimilated in the model. It appears clearly that the CAPE production fields exhibit negative areas that are consistent with the evolution of the convective activity seen on the satellite images of Figs. 3a,c,f,h, in the sense that where CAPE is produced (negative values in Fig. 7), convective activity subsequently increases, and where CAPE diminishes, convection subsequently collapses. The best example of this collocation is the global shape of the CAPE production field at 1200 UTC (Fig. 7b) that fairly corresponds to the cloud structure 6 h later (Fig. 3f). Let us consider again area A, characterized by a well-developed convective system at 1131 (Fig. 3c), which progressively dissipates in a region of negative CAPE (Fig. 4b). In this region, it is clearly shown that the CAPE production field provides the missing information

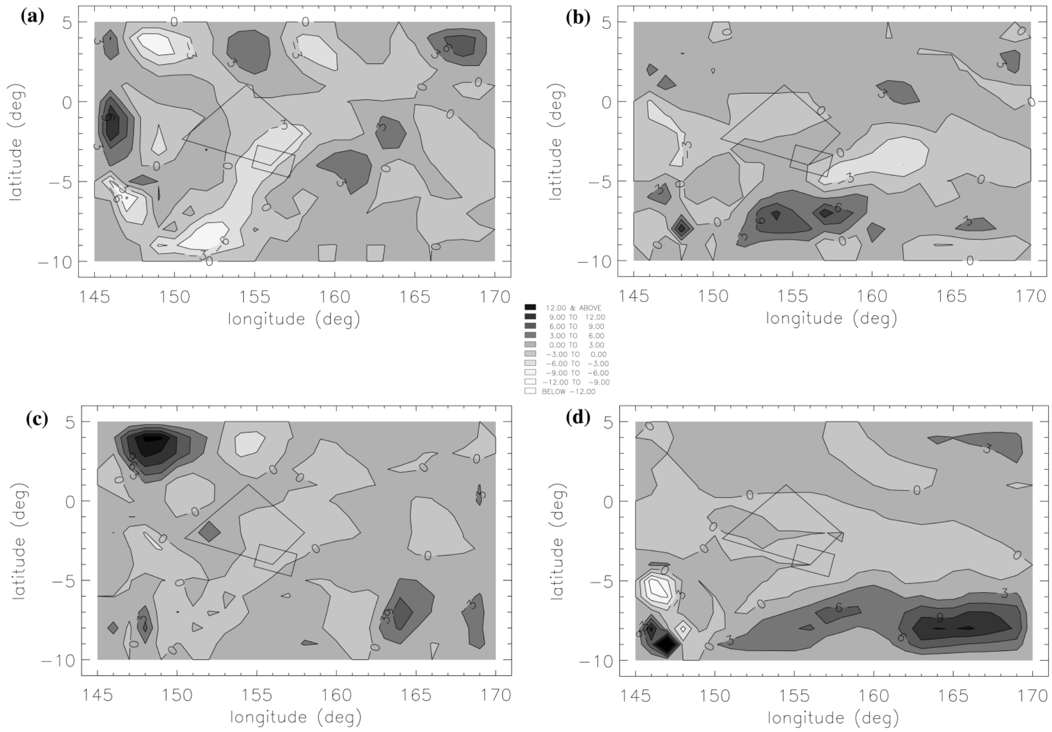

FIG. 8. Display of the terms of Eq. (A3) contributing to the CAPE production of Fig. 7b: (a) $-u\partial(\partial\theta_e/\partial z)/\partial x$, (b) $-v\partial(\partial\theta_e/\partial z)/\partial y$, (c) $-(\partial u/\partial z)(\partial\theta_e/\partial x)$, and (d) $-(\partial v/\partial z)(\partial\theta_e/\partial y)$.

to understand the observed inhibition of convective activity: a diminution of CAPE is diagnosed (Fig. 7b), which means that this region is no longer supplied with positive CAPE by the synoptic-scale circulation. This leads to the progressive decay of the convective activity in this area observed from Fig. 3d to Fig. 3f.

Let us now focus on the particular region where S developed. The field of CAPE tendency at 1200 (Fig. 7b) in this area shows that CAPE is produced at that time. Inspection of the GMS images at 1131 (Fig. 3c), 1331 (Fig. 3d), and 1631 (Fig. 3e) and the CAPE production field at 1200 (Fig. 7b) reveals that the convective entities roughly aligned along L1 and L2 (whose merging led to the development of S; see section 4); both propagate toward the same region of CAPE production located between them (denoted P1 in Fig. 7b). This strongly suggests that the existence of the P1 production area is the key factor to explain the merging of these convective entities and the subsequent intensification of S. The field of CAPE production at 1800 (Fig. 7c) shows that there is no more production of CAPE at this time in the S area, which indicates that the synoptic-scale circulation does not produce CAPE after 1800 UTC.

A further examination of the processes involved in the temporal evolution of CAPE in the S area is conducted in the following using the diagnostic equation (A3). The synoptic-scale contributions to this CAPE production area P1 [advection and differential advection terms on the right-hand side of (A3)] are displayed in Fig. 8. Comparison between these fields and the field of CAPE production at 1200 (Fig. 7b) in the P1 area shows that the advective term in the x direction [i.e., $-u\partial(\partial\theta_e/\partial z)/\partial x$; Fig. 8a] is the dominant term. This suggests a horizontal advection of positive CAPE from a region located farther west of the P1 area. Moreover, it is noted that the advective terms in the x and y directions (Figs. 8a and 8b, respectively) exhibit maximum values in a region that fairly corresponds to the location of the synoptic-scale convergence line of Fig. 5b, suggesting that positive CAPE is horizontally advected along this convergence line.

The propagation of the convective entities related to L1 and L2 toward the CAPE production area P1 is consistent with previous theoretical studies of squall lines. For instance, Lemaître and Testud (1986) demonstrated that this propagation toward convectively unstable regions helped maintain the supply of the system with unstable air, and ensured the vertical inversion of layers (overturning process) that acts in squall lines as a thermodynamic stabilizing process of the troposphere. The southwestward propagation of the squall line that forms on the northeastern part of the domain (whose location is indicated by an arrow in Figs. 3a–h) is another good illustration of this behavior. In fact, examination of the CAPE production fields at 0600, 1200, and 1800 UTC (Fig. 7), and of the respective locations of the squall line at these three time steps, clearly shows that the

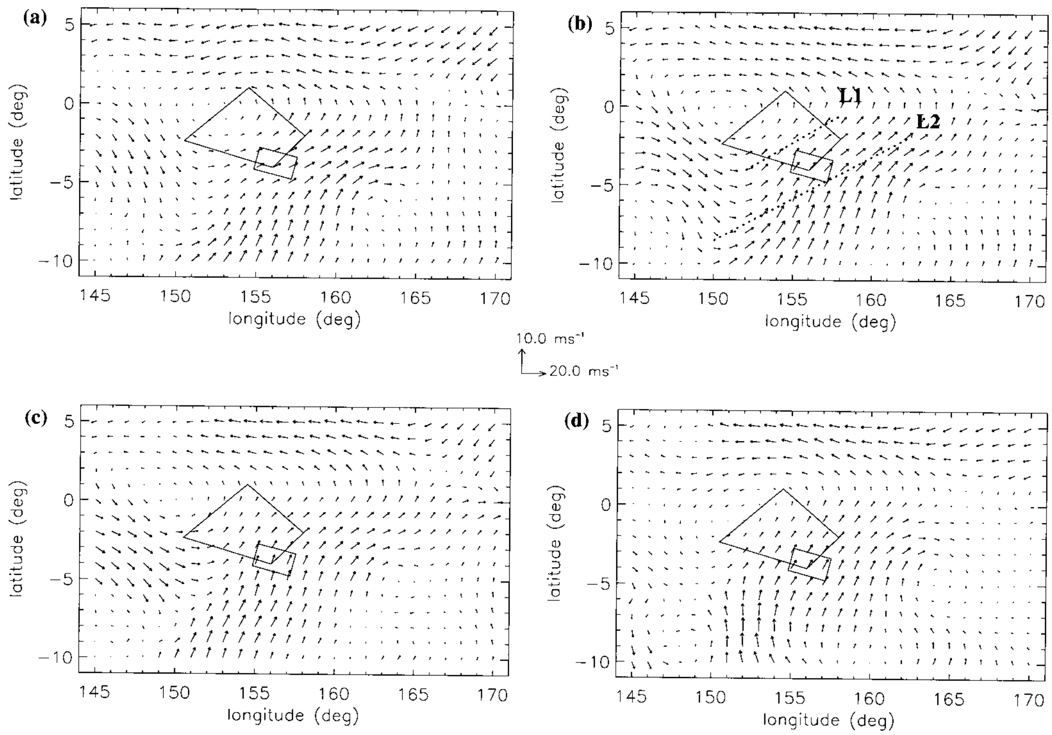

FIG. 9. Same as in Fig. 4 but for horizontal wind at 850 hPa.

southwestward propagation of the squall line is ‘‘driven’’ by a local maximum of CAPE production that is always located just ahead and southwest of the system. As long as this squall line moves, it must be noted also that a diminution of CAPE characterizes the rear part of the squall line (see in particular Fig. 7b), suggesting that the qualitative indicator used to estimate the CAPE tendency is in this case is a good tracer of the overturning process.

These fields of CAPE production (Fig. 7) may also be used to explain the stationarity of S observed in the satellite imagery during its development stage. Contrary to the squall line located in the northeastern part of the domain (Figs. 3b–h), S is collocated with the region of CAPE production, and the respective horizontal sizes of system S and of its associated region of CAPE production are fairly comparable. As a result, S does not have to propagate to reach ‘‘energetical’’ regions (unlike the squall line located farther northeast), as long as CAPE is produced by the synoptic-scale circulation (until 1800 UTC). It is also worth mentioning that once the overturning is achieved, S splits into two distinct groups of convective activity (Figs. 3f–h) that are both propagating toward areas of CAPE production (see Fig. 7d) surrounding (on the northwestern and southeastern sides) the primary CAPE area associated with S.

c. Synoptic-scale kinematic processes associated with the evolution of system S

The previous results indicate that the synoptic-scale circulation plays a major role in the initiation and general evolution of S. We will now examine the synoptic-scale processes associated with the time evolution of the convergence line in the S area. The convergence line at 850 hPa (Fig. 5) that intensifies from 0600 to 1800 and decreases from 1800 to 2400 is due to the confluence between a southwesterly flow (see Fig. 9, showing the horizontal wind at 850 hPa and at 0600, 1200, 1800, and 2400 UTC), whose origin and intensification are discussed in section 3, and a northwesterly flow that corresponds to the beginning of the second westerly wind burst episode of the COARE IOP (see section 3). The time evolution of the convergence line in Fig. 9 (enhancement of convergence from 0600 to 1800 and diminution from 1800 to 2400) is important to point out, because it is mainly imposed by the time evolution of the northwesterly flow. The time evolution of this northwesterly flow has been identified in turn to be connected to the time evolution of vertical vorticity at 700 hPa (Fig. 10). Indeed, the vertical vorticity field at 700 hPa exhibits a large positive maximum, associated with a well-defined anticyclonic circulation, denoted C in the following. This positive vertical vorticity maximum increases in magnitude from 0600 to 1800, and diminishes from 1800 to 2400. A longitudinal vertical cross section of vertical vorticity at 2°S and at 1200 UTC (not shown) indicates that this anticyclonic circulation C (Fig. 10) extends vertically from 850 up to 250 hPa. The observed consistency between the respective evolutions of vertical vorticity at 700 hPa and horizontal wind at 850 hPa suggests that the evolution of circulation C at 700

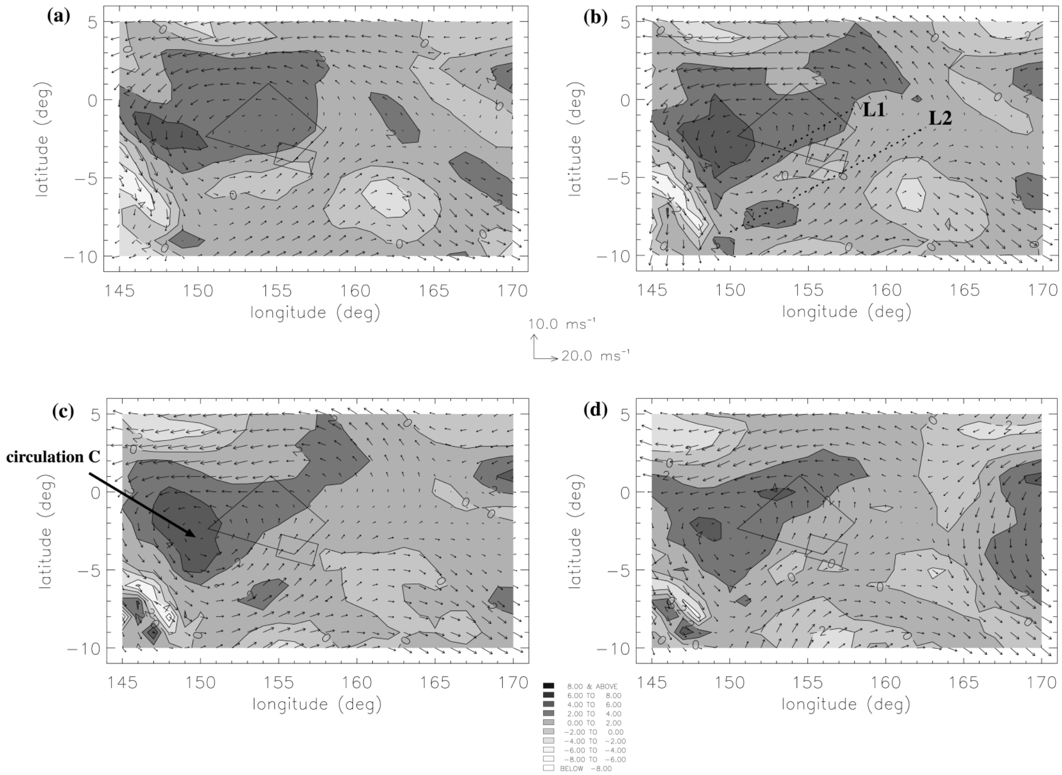

FIG. 10. Same as in Fig. 4 but for vertical vorticity at 700 hPa. Superimposed is the ECMWF analysis of the horizontal wind at 700 hPa. Also shown in (c) is the location of the anticyclonic circulation C discussed in the text.

hPa (Fig. 10) drives the evolution of the northwesterly flow at 850 hPa. This hypothesis is reinforced by inspection of the vertical vorticity field at 500 hPa, given in Fig. 11 for 0600, 1200, 1800, and 2400 UTC. A strong vorticity maximum is generated at 0600 (Fig. 11a), on the southern border of the easterly equatorial jet at 500 hPa characterized by a strong negative horizontal shear $\partial u/\partial y < 0$. This vorticity maximum propagates westward with the flow (see Figs. 11b–d), leading to a maximum at 1200 just above the vertical vorticity maximum at 700 hPa, and to a decrease from 1200 to 2400 at this location, while it propagates westward.

This maximum vertical vorticity at 500 hPa occurs prior to the maximum at 700 hPa. This result suggests that the evolution of vertical vorticity at 700 hPa is driven from aloft by the evolution of vertical vorticity at 500 hPa. To evaluate this hypothesis, the kinematic mechanisms leading to the intensification of vertical vorticity at 700 hPa can be studied using the diagnostic equation for vertical vorticity, which may be written as follows (e.g., Sui and Yanai 1986):

$$\frac{D\overline{\zeta}}{Dt} = (\overline{\zeta} + f)\frac{\partial\overline{w}}{\partial z} + \left(\overline{\xi}\frac{\partial\overline{w}}{\partial y} + \overline{\eta}\frac{\partial\overline{w}}{\partial x}\right) + Z'_s, \quad (1)$$

where (η, ξ, ζ) are the three components of the relative vorticity vector, f is the Coriolis parameter, overbars denote averaged parameters values resolved by the model, and Z'_s is a vorticity source due to eddy momentum transports by deep convection (subgrid-scale processes). As for the CAPE production in the appendix, our purpose with this diagnostic equation is to study the contribution of the synoptic-scale circulation to the evolution of vertical vorticity. Then, in the following, only the terms resolved by the model will be estimated and discussed in order to infer the process(es) involved at synoptic scale in this production, although it is well known that in deep convective situations, Z'_s is substantial, just as large as the other terms in (1).

Figure 12a shows the rate of change of vertical vorticity at 1200 UTC on a longitudinal W–E vertical cross section at 2°S. This field exhibits positive values below 500 hPa with two local maxima, corresponding to an increase of vertical vorticity with time. Above 500 hPa, it is diagnosed that vertical vorticity will diminish with time. The first production maximum below 500 hPa is located slightly east of circulation C, at about 155°E. It is associated with upward motions (see Fig. 12b, showing the vertical wind component). These upward motions are associated with the convective entities roughly oriented along L1, as shown by the GMS image at 1131 (Fig. 3c). It is noted that this vertical cross section of temporal evolution of vertical vorticity at 1200 UTC is consistent with the qualitative evolution of vertical vorticity observed horizontally at 700 and 500 hPa between

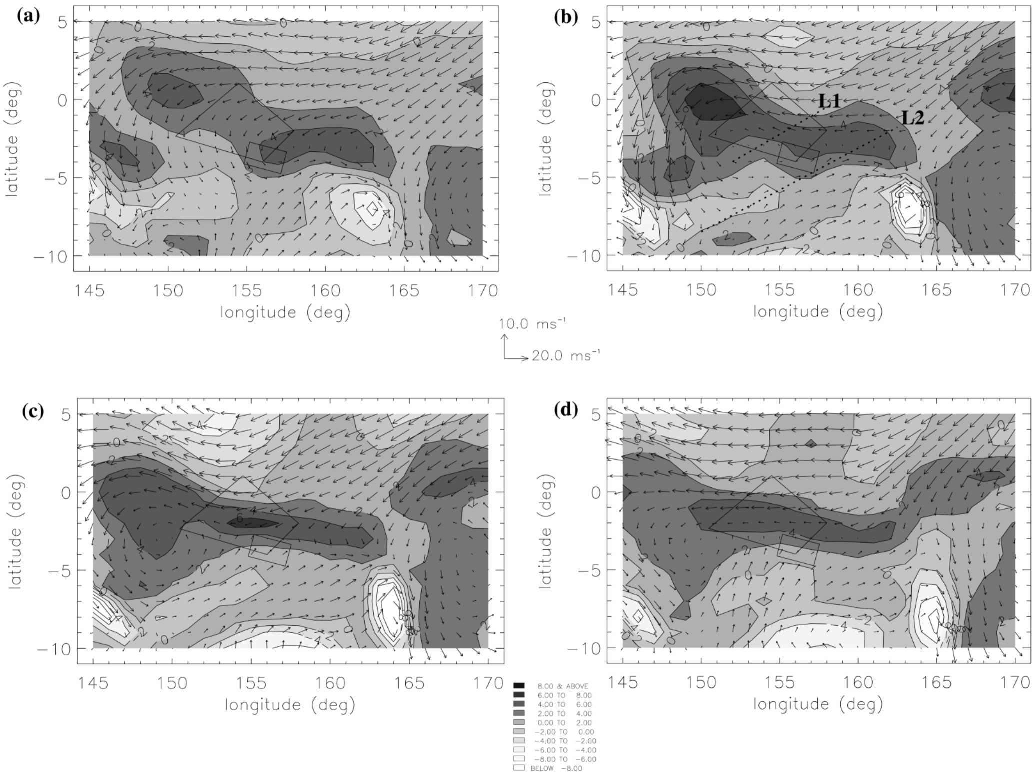

Fig. 11. Same as in Fig. 4 but for vertical vorticity at 500 hPa. Superimposed is the ECMWF analysis of the horizontal wind at 500 hPa.

1200 and 1800 UTC (see Figs. 10b,c and 11b,c). The second local production of vertical vorticity of Fig. 12a below 500 hPa is located farther east, at about 162°E. It is associated with a second region of upward motions (see Fig. 12b). Comparison with the GMS image of Fig. 3c shows that these upward motions are associated with the convective entities roughly aligned along L2.

The three terms contributing to the rate of change of vertical vorticity [terms on the right-hand side of (1)] are displayed in Figs. 12c–e, respectively. It is clearly seen from these figures that the first region of production associated with L1 is generated by both vertical stretching (Fig. 12e), due to the presence of deep convection in this area, and ''conversion'' of the y component of vorticity (Fig. 12d) into vertical vorticity (tilting of the vortex tubes from a given horizontal direction, here y, to the vertical), associated with horizontal gradients of w along the y axis. Vertical cross sections taken south of Fig. 12 (not shown) confirm the previous results, with a slight increase of the contribution of vertical stretching to the temporal evolution of vertical vorticity at 700 hPa. This result shows that deep convection interacts with the synoptic-scale circulation through the enhancement of vertical vorticity at 700 hPa. This interaction between circulation C (generated by the easterly jet at 500 hPa, as shown previously) and deep convection is therefore responsible for the progressive intensification of the convergence line (see again Fig. 5) and for the development of S. This shows the major role played by deep convection in the Tropics to trigger other convective systems remotely.

d. Potential vorticity and latent heat release

The vertical vorticity field and the terms contributing to its rate of change were examined in the previous section. Nevertheless, vertical vorticity is not a conservative quantity. In this section, the PV fields are therefore derived from the ECMWF outputs of vertical vorticity and potential temperature. The advantages of using such a parameter instead of vertical vorticity is that PV is conservative for adiabatic flows. The PV fields at 500 hPa and at 0600, 1200, 1800, and 2400 are given in Fig. 13. A large area of positive PV oriented along a W–E axis is found, within which more intense positive PV structures exist. This large positive PV area experiences an apparent westward propagation from 0600 to 2400 and gets progressively thinner during this westward propagation. Figure 13 also shows that the local positive PV area located initially at (3°S, 147°E) at 0600 (Fig. 13a) on the southern border of the vertical vorticity maximum at 700 hPa propagates southeastward. Comparison between these PV fields and the synoptic-scale horizontal wind at 500 hPa (Fig. 11) seems to indicate that the positive PV areas are advected by the synoptic-scale flow. In fact, the large positive PV area apparently

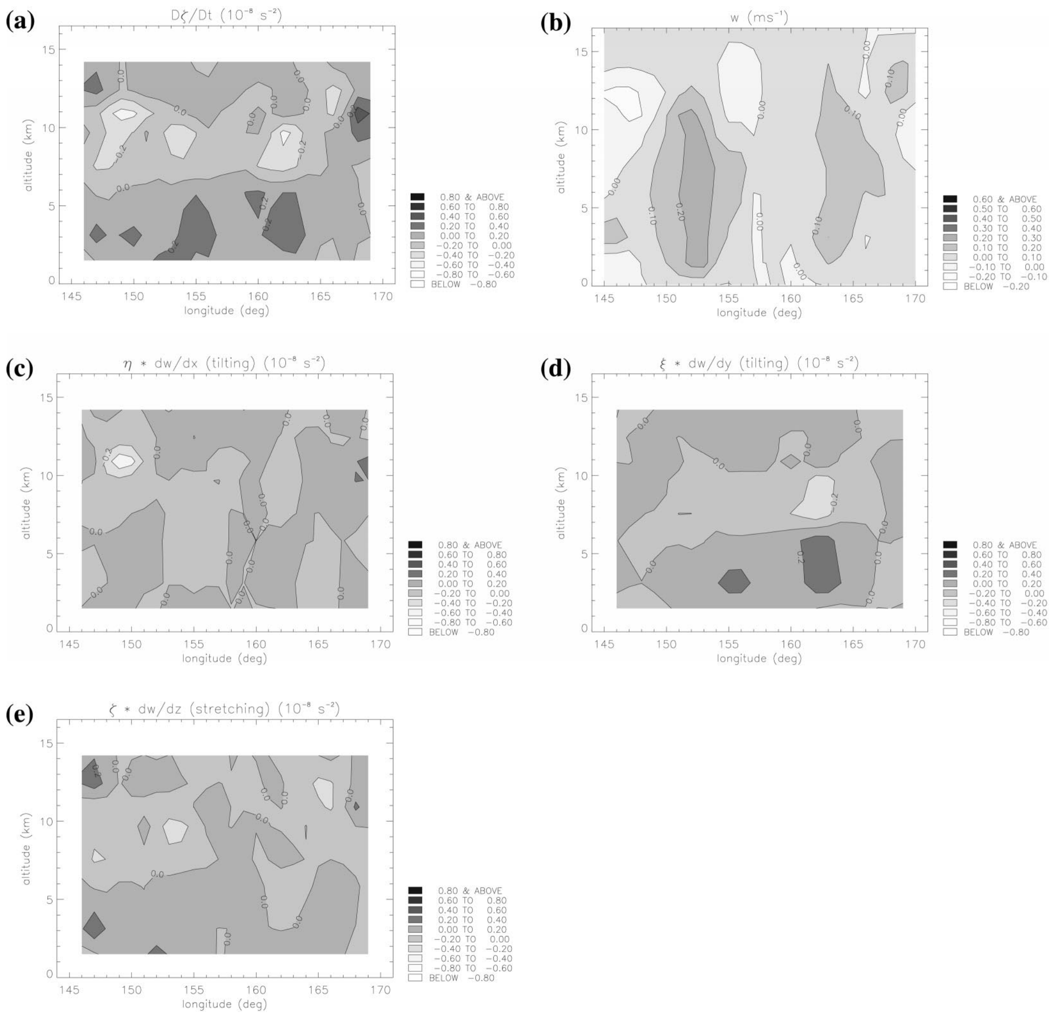

FIG. 12. Vertical cross section at 2°S and at 1200 UTC of (a) temporal evolution of vertical vorticity, (b) vertical velocity, and for the different terms contributing to the temporal evolution of vertical vorticity (c) $\eta\partial w/\partial x$, (d) $\xi\partial w/\partial y$, and (e) $\zeta\partial w/\partial z$.

propagates along the easterly equatorial jet at 500 hPa, while the local positive PV area located on the southern border of circulation C propagates along the northwesterly winds in this region. This hypothesis is confirmed by looking at the PV advection terms (not shown). In addition, this propagative behavior of the positive PV areas is also seen on the equivalent potential vorticity fields (computed as PV, but using θ_e instead of θ, not shown). Since this latter quantity is conserved for diabatic flows, it confirms the hypothesis that the PV and equivalent potential vorticity structures are advected by the synoptic-scale flow, rather than growing locally.

These PV fields show essentially the same temporal behavior as the vertical vorticity fields. Hence, interpretation of these fields is not carried out any further. However, since PV is conserved for adiabatic flows, the equation governing the Lagrangian temporal evolution of PV can be studied in further details so as to examine the importance of diabatic processes in the development of S. This equation may be written as (e.g., Bennets and Hoskins 1979)

$$\frac{D(PV)}{Dt} = \frac{1}{\rho}\boldsymbol{\nabla}\cdot\left(\theta\boldsymbol{\nabla}\times\mathbf{F} + \boldsymbol{\omega}\frac{D\theta}{Dt}\right), \qquad (2)$$

where $\mathbf{F}$ is the viscous force and $\boldsymbol{\omega}$ the relative vorticity vector. This equation shows that, following an air parcel, viscous and diabatic processes change θ and then change PV. It must be noted that it is the vertical derivative of latent heating or cooling rate that affects PV. Hence, in order to diagnose the condensation or evaporation processes using (2) (under the assumption that the only active diabatic processes are condensation and evaporation) the respective signs of the latent heating or cooling rate and of its vertical derivative must be known (e.g., Thorpe and Clough 1991). If both signs are positive (negative), (2) shows that condensation (evaporation) will increase (decrease) PV in a layer.

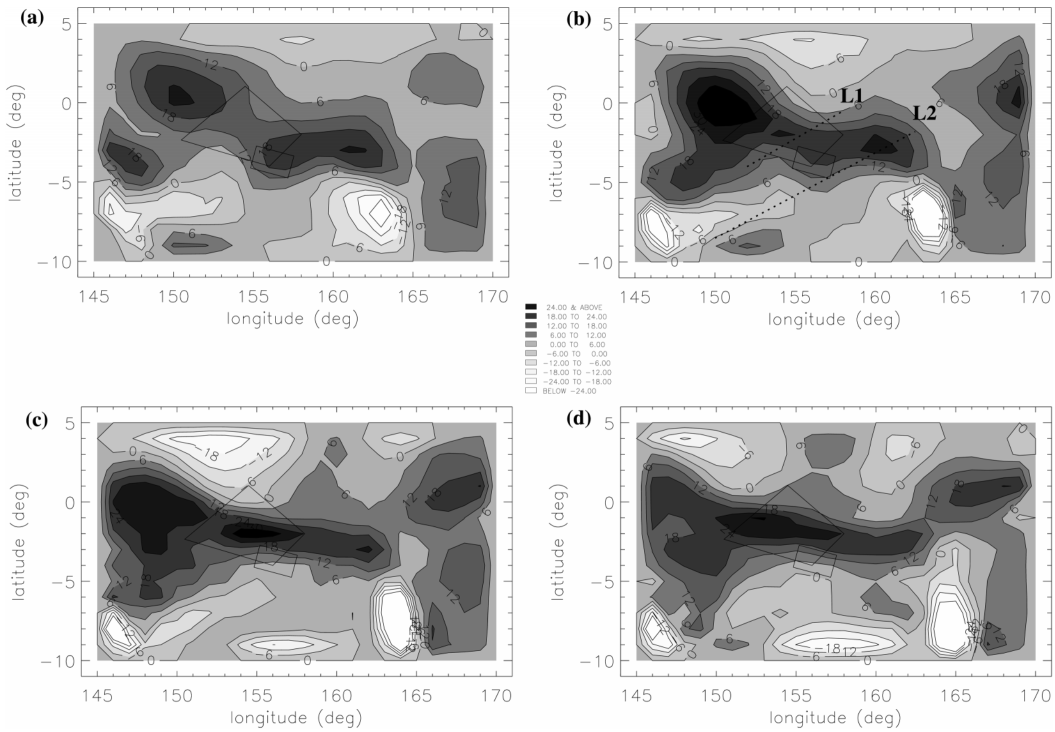

FIG. 13. Same as in Fig. 4 but for dry potential vorticity (PV) fields at 500 hPa.

Mapes and Houze (1995) showed that the vertical profile of divergence could be simply related to the diabatic heating profile in tropical convection. Their vertical profiles obtained using the TOGA COARE IOP database indicate that the heating rate is positive throughout the troposphere, with a maximum located between 8- and 10-km height in convective areas during COARE (associated with peak upward motions close to the tropopause), which is higher than the 500-hPa level generally observed (see review by Webster and Lukas 1992). Using airborne Doppler radar data, Protat et al. (1997) estimated vertical profiles of divergence and vertical air motion within the 15 December 1992 MCS of COARE (see their Fig. 13), which is the case studied in the present paper. Their results, following Mapes and Houze (1995), show a maximum latent heat release around 8-km altitude for convective and stratiform regions, and a maximum cooling around 1–2-km altitude. Then, for the 15 December 1992 case, the vertical derivative of latent heating rate is positive from 1–2-km height up to 8–10-km height. This implies that within the 2–8-km vertical layer, PV production is associated with the presence of condensation, while PV diminution is the signature of evaporation processes.

We now turn to an examination of condensation–evaporation signatures associated with system S using the diagnostic equation (2). The local time derivative of PV between two ECMWF analyses is simply estimated using the difference fields of PV between two time steps, and the advective terms of the equation are estimated using the ECMWF fields at a given time step. The Lagrangian time derivative of PV at 700 hPa and at 1200 is given in Fig. 14. In the area where S develops (see Figs. 3d–f), it appears clearly that the most active part of S (located on its southeastern border) is characterized by condensation, as shown by the local production of PV in Fig. 14 around (5.5°S, 155°E) and (3.5°S, 156°E) (right in the middle of the mesoscale domain given in Fig. 14). In contrast, the rear part of the system (corresponding to decaying convective cells that progressively move northeastward) is characterized by evaporation, as suggested by the slight local PV sink around (2°S, 156°E) in Fig. 14. It should be noted as well that (i) the vertical velocity field at 700 hPa (not shown) is consistent with this condensation–evaporation structure, which indirectly confirms the quality of these PV fields, and (ii) more generally, the temporal evolution of PV is in very good agreement with the evolution of the several convective systems observed on the brightness temperature fields of Fig. 3. In fact, the systems that intensify are mostly associated with a PV production, while the decaying systems are associated with a PV diminution.

6. Summary and conclusions

In this paper, the synoptic-scale context associated with the initiation and evolution of the 15 December 1992 cloud cluster observed during COARE is examined. This study makes use of the ECMWF model out-

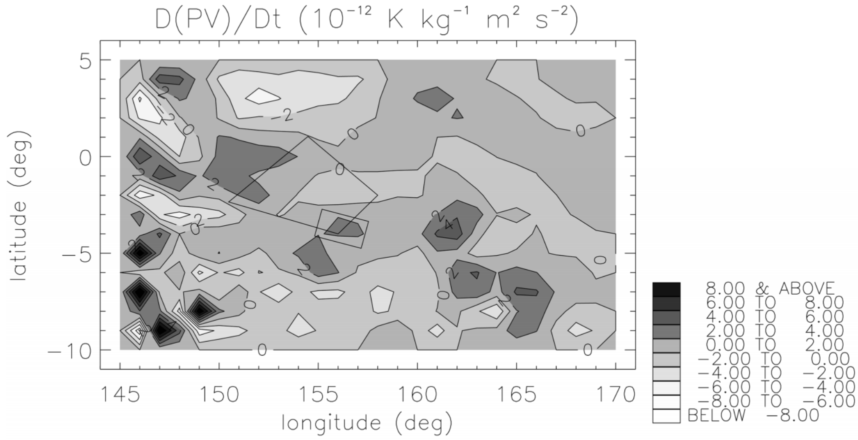

FIG. 14. Lagrangian derivative of PV at 700 hPa at 1200 UTC. This field is equivalent to the diabatic and frictional sources of dry potential vorticity.

puts and *GMS-4* satellite imagery in the infrared channel. The quality of the ECMWF fields for 15 December 1992 is first assessed. It is recalled that the 15 December 1992 convective system developed when westerly winds began to appear in the lowest tropospheric layers, 2 weeks prior to the peak westerlies associated with the second major westerly wind burst episode of COARE. The presence of active phase of MJO is also identified.

Two types of conclusions may be drawn from the present study. The first type of conclusion concerns the synoptic-scale mechanisms involved in the initiation and evolution of the studied cloud cluster. The second type concerns the general behavior of MCSs and associated deep convection in terms of propagation and organization. From the ECMWF outputs at 0600 and 1200, a particular region is identified as strongly favorable for the development of deep convection, with (i) a strong low-level confluence at 850 hPa and below between a northwesterly flow (associated with the westerly wind burst episode) and a southwesterly flow, (ii) strong CAPE from 1200 to 1800, and (iii) strong production of CAPE at 1200. This favorable region corresponds to the area where S formed, which shows that the synoptic-scale circulation and dynamic features provide the initial conditions for the formation of S. In addition, the evolution of the CAPE and divergence fields in time is clearly found to be linked to the evolution of the convective activity associated with S. This shows that the evolution of the synoptic-scale dynamic characteristics governs the general evolution of S.

It is also shown that initially, north from S, an easterly equatorial jet at 500 hPa generates positive ζ and PV on its southern border at 0600 UTC, due to the important horizontal wind shear in this region. Then, these positive ζ and PV structures propagate westward with the flow at 500 hPa, leading to the generation of an anticyclonic circulation C, vertically extending from 850 up to 250 hPa and with a peak magnitude at 1200 at 500 hPa and at 1800 at 700 hPa. Vortex stretching and tilting of the horizontally oriented vortex tubes along the *y* axis to the vertical are evidenced as the main processes involved in the intensification of this circulation C at 700 hPa from 0600 to 1800. This result implies that deep convection and associated vertical motions interact with the synoptic-scale circulation. This intensification of vertical vorticity at 700 hPa promotes in turn the intensification of the low-level northwesterly flow from 0600 to 1800 and hence the intensification of the synoptic-scale low-level convergence line responsible for the general evolution of S. From 1800, the magnitude of vertical vorticity associated with circulation C decreases at 700 hPa, inducing the diminution of the synoptic-scale convergence. At the same time, no more CAPE is produced in this area. These two major changes in the synoptic-scale dynamic characteristics around the location of S are clearly responsible for the dissipation of S.

More generally, some noticeable results about deep convection and mesoscale convective systems are obtained in this study. First, it is confirmed that convective systems tend to propagate toward regions of CAPE production. This particular process clearly explains (i) the morphological initiation of system S resulting from the propagation of two initial groups of convective entities toward the same region of strong CAPE and CAPE production, (ii) the southwestern propagation of a squall line located northeast of S toward another area of CAPE production, and (iii) the quasi-nil propagation of S. With respect to point iii, it is postulated that S does not have to propagate as long as the synoptic-scale circulation provides both low-level convergence and CAPE in the same area, since the size and location of the energy area is approximately the same as the size and location of the MCS itself. In Part II, the downscale interaction processes (i.e., from synoptic scale to mesoscale and convective scale) are investigated, as well as the dynamic and thermodynamic mechanisms involved in the internal organization of the 15 December 1992 MCS on the mesoscale and convective scale. This study uses both the synoptic-scale context described in the present paper and the P3 airborne Doppler radar measurements collected within S from 1700 to 2100 UTC.

Acknowledgments. The radiosounding data were obtained from the TOGA COARE International Project Office (UCAR, Boulder, CO). Catherine Piriou and Mathieu Nuret helped extract the GMS satellite images from the TOGA COARE database at Météo-France (Toulouse, France). The GMS data were made available by Dr. T. Nakazawa. The NCAR ZEB software was used to construct Fig. 3. Financial support for the French participation in the COARE field experiment was provided by Institut National des Sciences de l'Univers Grants/PATOM 95/15 and 96/02.

APPENDIX

Rate of Change of CAPE and Contributing Terms

If one assumes that the only diabatic effects that act on the air parcels are the condensation and evaporation processes, then θ_e is conserved. This conservative property may be written as

$$\frac{D\theta_e}{Dt} = 0, \tag{A1}$$

where $D/Dt = \partial/\partial t + u(\partial/\partial x) + v(\partial/\partial y) + w(\partial/\partial z)$ is the Lagrangian time derivative following an air parcel. Differentiating (A1) with respect to z leads to

$$\frac{\partial}{\partial z}\left(\frac{D\theta_e}{Dt}\right) = 0 = \underbrace{\frac{\partial}{\partial t}\left(\frac{\partial\theta_e}{\partial z}\right)}_{(1)} + \underbrace{u\frac{\partial}{\partial x}\left(\frac{\partial\theta_e}{\partial z}\right) + v\frac{\partial}{\partial y}\left(\frac{\partial\theta_e}{\partial z}\right) + w\frac{\partial}{\partial z}\left(\frac{\partial\theta_e}{\partial z}\right)}_{(2)} + \underbrace{\frac{\partial u}{\partial z}\frac{\partial\theta_e}{\partial z} + \frac{\partial v}{\partial z}\frac{\partial\theta_e}{\partial y} + \frac{\partial w}{\partial z}\frac{\partial\theta_e}{\partial z}}_{(3)}, \tag{A2}$$

where term 1 is the local time evolution of the vertical gradient of θ_e, terms 2 are the advective terms indicating the displacement of energy in a given direction, and terms 3 are the differentially advective terms, expressing the generation of CAPE through differential displacement with altitude of thermodynamically distinct air masses, leading to a vertical superposition of air masses favorable for the development of convection. The local time derivative of the vertical gradient of θ_e may then be isolated in (A2), leading to a qualitative estimate of the "CAPE production."

It must be noted that when using model outputs in this diagnostic equation, a complete balance of (A2) requires an accounting of the subgrid-scale terms [i.e., the convective source terms of (A2)] parameterized in the model. Each of the variables may then be decomposed as the sum of an average value corresponding to the scale resolved by the model and an eddy term corresponding to scales that are not resolved by the model.

This leads to the following expression for (A2):

$$\frac{\partial}{\partial t}\left(\frac{\partial\overline{\theta}_e}{\partial z}\right) = -\overline{u}\frac{\partial}{\partial x}\left(\frac{\partial\overline{\theta}_e}{\partial z}\right) - \overline{v}\frac{\partial}{\partial y}\left(\frac{\partial\overline{\theta}_e}{\partial z}\right) - \overline{w}\frac{\partial}{\partial z}\left(\frac{\partial\overline{\theta}_e}{\partial z}\right) - \frac{\partial\overline{u}}{\partial z}\frac{\partial\overline{\theta}_e}{\partial x} - \frac{\partial\overline{v}}{\partial z}\frac{\partial\overline{\theta}_e}{\partial y} - \frac{\partial\overline{w}}{\partial z}\frac{\partial\overline{\theta}_e}{\partial z} + Q'_S, \tag{A3}$$

where overbars denote averaged parameter values resolved by the model and the term Q'_S groups all the subgrid-scale convective source terms that are not resolved by the model. Since our purpose in this paper is to evaluate the role played by the synoptic-scale circulation (and only by the synoptic-scale circulation) in the generation of regions particularly favorable for the development of convection, it has naturally been chosen to focus on the terms of (A3) that are representative of the scale resolved by the model, although it is well known that the eddy convective source terms can be as large as the other terms in (A3) (Yanai et al. 1973, among others). Then, the tendency term on the left-hand side and the different terms on the right-hand side of (A3) except Q'_S are estimated using the raw ECMWF fields, in order to diagnose the local evolution of CAPE at synoptic scale and to identify the synoptic-scale processes involved in this evolution. Computation of these different terms (not shown) demonstrates that, in the areas of deep convection, the main term is $-\overline{w}\partial(\partial\overline{\theta}_e/\partial z)/\partial z$, that is, the term related to vertical transports. Since only convection is responsible for vertical transports in tropical regions, the synoptic-scale circulation can be assumed as purely horizontal. Hence, in order to study only the role played by the synoptic-scale circulation in the development and organization of convection, the discussion in section 5 only focuses on the contribution of the terms related to horizontal advection and differential advection, that is, the synoptic-scale contributions to the organization of the studied cloud cluster. The capabilities of the resulting quantity to describe qualitatively the evolution of CAPE at the synoptic scale is evaluated in section 5 by comparing the qualitative evolution of the convective activity predicted by this quantity with that observed in the satellite imagery.

REFERENCES

Bennets, D. A., and B. J. Hoskins, 1979: Conditional symmetric instability—A possible explanation for frontal rainbands. *Quart. J. Roy. Meteor. Soc.*, **105,** 945–962.

Bonnissent, J., C. Walker, N. Ascensio, M. Chong, J.-P. Lafore, M.

Nuret, P. Pires, and J.-L. Redelsperger, 1993: L'expérience TOGA-COARE: Suivi de la période d'observations intensives pour la composante atmosphérique. *La Météorologie,* **8,** 33–40.

Caillault, K., A. Protat, and Y. Lemaître, 1998: Multi-scale interactions involved in the life cycle of MCSs observed during TOGA-COARE. *Proc. COARE98 Conf.,* Boulder, CO, World Climate Research Programme (WCRP-107), 405–406.

Charney, J. G., and A. Eliassen, 1964: On the growth of the hurricane depression. *J. Atmos. Sci.,* **21,** 68–74.

Chen, S. S., and R. A. Houze Jr., 1997: Diurnal variation of deep convective systems over the tropical pacific warm pool. *Quart. J. Roy. Meteor. Soc.,* **123,** 357–388.

——, ——, and B. E. Mapes, 1996: Multiscale variability of deep convection in relation to large-scale circulation in TOGA COARE. *J. Atmos. Sci.,* **53,** 1380–1409.

Gutzler, D. S., G. N. Kiladis, G. A. Meehl, K. M. Weickmann, and M. Wheeler, 1994: The global climate of December 1992–February 1993. Part II: Large-scale variability across the tropical western Pacific during TOGA COARE. *J. Climate,* **7,** 1606–1622.

Hayashi, Y., 1970: A theory of large-scale equatorial waves generated by condensation heat and accelerating the zonal wind. *J. Meteor. Soc. Japan,* **48,** 140–160.

Hendon, H. H., and M. L. Salby, 1994: The life cycle of the Madden–Julian oscillation. *J. Atmos. Sci.,* **51,** 2225–2237.

Hildebrand, P. H., and C. K. Mueller, 1985: Evaluation of meteorological airborne Doppler radar. Part I: Dual-Doppler analyses of air motions. *J. Atmos. Oceanic Technol.,* **2,** 362–380.

Hollingsworth, A., 1994: Validation and diagnosis of atmospheric models. *Dyn. Atmos. Oceans,* **20,** 227–246.

Johnson, R. H., P. E. Ciesielski, and K. A. Hart, 1996: Tropical inversions near the 0°C level. *J. Atmos. Sci.,* **53,** 1838–1855.

Jorgensen, D. P., P. H. Hildebrand, and C. L. Frush, 1983: Feasibility test of an airborne pulse-Doppler meteorological radar. *J. Climate Appl. Meteor.,* **22,** 744–757.

Lemaître, Y., and J. Testud, 1986: Observation and modelling of tropical squall lines observed during the COPT 79 experiment. *Ann. Geophys.,* **4B,** 21–36.

Liebmann, B., and H. H. Hendon, 1990: Synoptic-scale disturbances near the equator. *J. Atmos. Sci.,* **47,** 1463–1479.

Lin, X., and R. H., Johnson, 1996: Kinematic and thermodynamic characteristics of the flow over the western Pacific warm pool during TOGA COARE. *J. Atmos. Sci.,* **53,** 695–715.

Luther, D. S., D. E. Harrison, and R. A. Knox, 1983: Zonal winds in the central equatorial Pacific and El-Niño. *Science,* **222,** 327–330.

Madden, R. A., and P. R. Julian, 1971: Detection of a 40–50 day oscillation in the zonal wind in the tropical Pacific. *J. Atmos. Sci.,* **28,** 702–708.

——, and ——,1972: Description of global-scale circulation cells in the tropics with 40–50 day period. *J. Atmos. Sci.,* **29,** 1109–1123.

——, and ——,1994: Observations of the 40–50-day tropical oscillation—A review. *Mon. Wea. Rev.,* **122,** 814–837.

Mapes, B. E., and R. A. Houze, Jr., 1993: Cloud clusters and superclusters over the oceanic warm pool. *Mon. Wea. Rev.,* **121,** 1398–1415.

——, and ——,1995: Diabatic divergence profiles in western Pacific mesoscale convective systems. *J. Atmos. Sci.,* **52,** 1807–1828.

——, and P. Zuidema, 1996: Radiative-dynamical consequences of dry tongues in the tropical atmosphere. *J. Atmos. Sci.,* **53,** 620–638.

McBride, J. L., N. E. Davidson, K. Puri, and G. C. Tyrell, 1995: The flow during TOGA COARE as diagnosed by the BMRC tropical analysis and prediction system. *Mon. Wea. Rev.,* **123,** 717–736.

Nakazawa, T., 1988: Tropical super clusters within intraseasonal variations over the western Pacific. *J. Meteor. Soc. Japan,* **66,** 823–839.

——, 1995: Intraseasonal oscillations during the TOGA-COARE IOP. *J. Meteor. Soc. Japan,* **73,** 305–319.

Numaguti, A., R. Oki, K. Nakamura, K. Tsuboki, N. Misawa, T. Asai, and Y.-M. Kodama, 1995: 4–5 day period variations and low-level dry air observed in the equatorial western Pacific during the TOGA-COARE IOP. *J. Meteor. Soc. Japan,* **73,** 267–290.

Nuret, M., and M. Chong, 1996: Monitoring the performance of the ECMWF operational analysis using the enhanced TOGA COARE observational network. *Wea. Forecasting,* **11,** 53–65.

Pires, P., J. L. Redelsperger, and J. P. Lafore, 1997: Equatorial atmospheric waves and their association to convection. *Mon. Wea. Rev.,* **125,** 1167–1184.

Protat, A., and Y. Lemaître, 2001: Scale interactions involved in the initiation, structure, and evolution of the 15 December 1992 MCS observed during TOGA COARE. Part II: Mesoscale and convective-scale processes. *Mon. Wea. Rev.,* **129,** 1779–1808.

——, ——, and G. Scialom, 1997: Retrieval of kinematic fields using a single-beam airborne Doppler radar performing circular trajectories. *J. Atmos. Oceanic Technol.,* **14,** 769–791.

Rickenbach, T. M., and S. A. Rutledge, 1998: Convection in TOGA COARE: Horizontal scale, morphology, and rainfall production. *J. Atmos. Sci.,* **55,** 2715–2729.

Salby, M. L., R. R. Garcia, and H. H. Hendon, 1994: Planetary-scale circulations in the presence of climatological and wave-induced heating. *J. Atmos. Sci.,* **51,** 2344–2367.

Sui, C.-H., and M. Yanai, 1986: Cumulus ensemble effects on the large-scale vorticity and momentum field of GATE. Part 1: Observational evidence. *J. Atmos. Sci.,* **43,** 1618–1642.

——, and K.-M. Lau, 1992: Multiscale phenomena in the tropical atmosphere over the western Pacific. *Mon. Wea. Rev.,* **120,** 407–430.

Takayabu, Y. N., and T. Nitta, 1993: 3–5 day period disturbances coupled with convection over the tropical Pacific Ocean. *J. Meteor. Soc. Japan,* **71,** 221–246.

——, K.-M. Lau, and C.-H. Sui, 1996: Observation of a quasi-2-day wave during TOGA COARE. *Mon. Wea. Rev.,* **124,** 1892–1913.

Thorpe, A. J., and S. Clough, 1991: Mesoscale dynamics of cold fronts: Structures described by dropsoundings in Fronts 87. *Quart. J. Roy. Meteor. Soc.,* **117,** 903–941.

Webster, P. J., and R. Lukas, 1992: TOGA COARE: The Coupled Ocean–Atmosphere Response Experiment. *Bull. Amer. Meteor. Soc.,* **73,** 1377–1415.

Yanai, M., S. Esbensen, and J. H. Chu, 1973: Determination of bulk properties of tropical cloud clusters from large-scale heat and moisture budgets. *J. Atmos. Sci.,* **30,** 611–627.

Young, J. A., and D. N. Sikdar, 1973: A filtered view of fluctuacting cloud patterns in the tropical Pacific. *J. Atmos. Sci.,* **30,** 392–407.

Zipser, E. J., and R. H. Johnson, 1998: Systematic errors in radiosonde humidities: A global problem? Preprints, *10th Symp. on Meteorological Observations and Instrumentation,* Phoenix, AZ, Amer. Meteor. Soc., 72–73.